EarthArXiv Preprint Cover Sheet

Title

Undrained fault-zone poroelastic feedback enables the 2011 Prague earthquake cascade

Authors

Zhengze Li [1,*] , Sylvain Barbot [1]

Affiliations

[1] Department of Earth Sciences, University of Southern California, Los Angeles, CA, USA

Correspondence

Zhengze Li (zhengzel@usc.edu)

Preprint status statement

This manuscript is a non-peer-reviewed preprint submitted to EarthArXiv.

The manuscript is currently under editorial consideration at *Science Advances*.

Undrained fault-zone poroelastic feedback enables the 2011 Prague earthquake cascade

Zhengze Li[1*], Sylvain Barbot[1]

[1]Department of Earth Sciences, University of Southern California,

Los Angeles, California, USA. *Corresponding author. Email: zhengzel@usc.edu

Subsurface fluid injection supports wastewater disposal, geothermal energy, and geological storage but can trigger damaging earthquakes. Predicting whether an injection-triggered rupture stops or spreads across multiple faults remains challenging. In the 2011 Prague, Oklahoma, sequence, the mechanism enabling rupture transfer to the fault hosting the third large earthquake has remained unresolved. Here we build an observation-constrained model linking pore-pressure diffusion, frictional fault slip, elastic stress interactions, and a local undrained fault-zone poroelastic response. The model reproduces nearly 18 years of hydraulic buildup and the complete three-event sequence. Rupture of the second fault loads the third fault favorably in shear but also increases normal compression that inhibits slip. In our simulations, favorable shear loading develops into dynamic rupture on the third fault only when undrained fault-zone poroelastic feedback offsets enough of the opposing clamping. Hydraulic properties shape the timing and location of rupture initiation, and greater source–fault separation substantially delays it. After rupture begins, network prestress, geometry, and elastic interactions increasingly determine whether rupture spreads and which faults participate.

These results reveal two-way hydromechanical coupling in induced-earthquake sequences: injection governs hydraulic preparation, while rupture-induced stress changes feed back on fault-zone pore pressure and subsequent fault stability.

Introduction

Subsurface fluid injection is integral to wastewater disposal associated with hydrocarbon production, geothermal energy development, hydraulic stimulation, and geological CO_2 and energy storage, but has increased seismicity in several continental regions and, in some cases, triggered damaging earthquakes (*1*). Managing this hazard is important for protecting communities and infrastructure and for enabling the safe deployment and public acceptance of subsurface technologies needed for energy production and the transition toward net-zero emissions (*2–4*). Induced seismicity also offers a rare opportunity to examine how documented anthropogenic perturbations interact with tectonically loaded faults. The principal triggering mechanisms are increasingly well established. Elevated pore pressure reduces effective normal stress, while poroelastic deformation, aseismic slip, and earthquake-mediated stress transfer can load faults within or beyond the directly pressurized region (*1, 3, 5–10*).

Predicting which operations will generate seismicity, which faults will rupture, and how large those events will become remains challenging. Similar operations produce outcomes ranging from no detectable seismicity to damaging earthquakes, and injection rate or volume alone cannot explain this variability (*2, 3, 11*). Injection supplies a perturbation, but damaging earthquakes release preexisting tectonic strain energy. Dynamic-rupture theory shows that hydraulically initiated rupture may remain self-arrested or become runaway depending on prestress, frictional conditions, and available fault dimensions (*12, 13*). In a natural fault network, subsequent evolution may additionally depend on stress transfer, slip-induced poroelastic pressure changes, and the geometry and stability margins of neighboring faults (*14–16*). The central hazard question is therefore when an induced instability remains localized and when it transfers among faults to develop into a multi-fault rupture cascade. Addressing this question requires models that connect years of hydraulic loading, hours to days of frictional nucleation and rupture transfer, and the longer-term response of the surrounding fault network.

The 2011 Prague, Oklahoma, sequence has become a canonical example of consequential induced seismicity (*2*). Its three-event cascade provides a natural test of how induced rupture transfers through a fault network. After nearly 18 years of continuous wastewater disposal, an M_w 5.0 foreshock, an M_w 5.7 mainshock, and a subsequent M_w 5.0 event ruptured distinct segments of the Wilzetta fault system within about three days (Figure 1; 17, 18). The mainshock occurred approximately one day after the foreshock, and the third event followed approximately two days later. Mapped fault traces, relocated seismicity, and focal mechanisms reveal a geometrically complex basement fault system rather than a single planar rupture (*18–22*). The disposal intervals lie within the sedimentary section above crystalline basement, whereas the three large earthquakes occurred in the basement at depths of approximately 2.5–3.4 km (Figure 1B; 18).

Previous studies linked long-term injection to the first event and showed that the static coseismic stress change from that event favored the mainshock (*17, 18*). This explanatory chain does not extend to the third event. Its fault was previously interpreted as unfavorably oriented under the preferred regional stress direction (*22*), and static stress-change calculations did not show that the first two events favored its occurrence (*18*). A recent physics-based fault-network simulation reproduced the first two large events but not the third (*23*). A successful explanation of the complete sequence therefore must account for how rupture transferred to Fault 3.

Here, we construct an observation-constrained model of the Prague fault network. Injection-driven pressure diffuses through the host rock and preferentially along fault zones, fault resistance evolves with slip velocity and fault state, and slip transfers shear and normal stresses among faults. The model also represents an undrained fault-zone poroelastic response, in which slip-induced normal-stress changes alter pore pressure and thereby feed back on effective normal stress and fault stability. After reproducing the event order, timing, approximate magnitudes, and rupture extents, we examine how hydraulic properties, operational forcing, and the initial fault stress govern the approach to instability. We then test how this poroelastic feedback affects rupture transfer to Fault 3 and how prestress, geometry, and elastic interactions govern activation of the surrounding fault network. Together, these experiments distinguish the controls on rupture initiation, inter-fault transfer, and further escalation through a fault network.

Model and Experimental Design

Observation-constrained fault networks and hydraulic loading

We represent the Prague fault system in a two-dimensional horizontal plane and connect injection-induced pressure changes to frictional slip on interacting faults. The calculations in Figures 2–4 use three fault segments corresponding to the principal ruptures of the 2011 sequence. Their locations and orientations are constrained by mapped traces, relocated seismicity, focal mechanisms, and published rupture interpretations (*17, 20–22*). The post-sequence calculations in Figure 5 extend the same approach to 27 mapped segments of the Wilzetta fault system. Exact fault coordinates, discretization, and model parameters are reported in tables S1–S4.

Under the assumption of a homogeneous, isotropic poroelastic full space, mechanical equilibrium and fluid mass conservation with Darcy flow reduce to a pressure diffusion equation with spatially variable permeability (*24*). We solve the resulting equation on an adaptive finite-volume grid:

$$\frac{\partial P}{\partial t} = \nabla \cdot (D \nabla P) + s_P(\mathbf{x}, t), \tag{1}$$

where D is hydraulic diffusivity and s_P is the pressure-rate source term representing injection. The grid explicitly contains 200-m-wide high-diffusivity corridors centered on the modeled faults. In the reference simulations, their diffusivity is 1000 times the host-rock value, allowing pressure to migrate preferentially along the fault network rather than through a homogeneous medium. The calculated injection-pressure history P_{inj} is sampled at every fault element and reduces effective normal stress. The source location and reference volumetric injection rate are based on the well records of Keranen et al. (*17*). We convert the volumetric rate to an equivalent two-dimensional source rate using an effective out-of-plane flow thickness of approximately 1.8 km. The numerical grid, source conversion, boundary conditions, and hydraulic benchmark are described in the supplementary Materials and Methods (*24*) and fig. S1.

Frictional slip and elastic fault interactions

We model fault slip by coupling evolving frictional resistance with elastic stress interactions within and among faults. The friction coefficient depends on slip velocity and a state variable that evolves with time and slip. We use the following friction law (*25*):

$$f = f_0 \exp\left[\frac{a}{f_0} \ln\left(\frac{V}{V_0}\right) + \frac{b}{f_0}\Phi\right], \tag{2}$$

with state evolution

$$\dot{\Phi} = \frac{V_0 e^{-\Phi} - V}{L}. \tag{3}$$

Here, f is the friction coefficient, V is slip velocity, V_0 is the reference slip velocity, and f_0 is the friction coefficient at $V = V_0$ and $\Phi = 0$. The dimensionless parameters a and b describe the direct velocity and state effects, respectively, and L is the characteristic state-evolution distance. The dimensionless state variable is defined as $\Phi = \ln(\theta V_0/L)$, where θ is a state variable with units of time. Most fault interiors are assigned velocity-weakening friction to permit unstable slip, whereas velocity-strengthening transitions are imposed near selected fault tips to promote rupture arrest. Slip is governed by the quasi-dynamic force balance

$$\tau = \sigma_n' f + \eta V, \tag{4}$$

where τ is shear stress, σ_n' is effective normal stress, and η is the radiation-damping coefficient. This formulation allows the same fault system to evolve from slow interseismic motion through nucleation to dynamic rupture. Frictional parameter values and the spatial construction of the velocity-strengthening tip transitions are given in the supplementary Materials and Methods (*24*).

Slip on every element changes both shear and total normal stress throughout the fault network. For the slip vector δ, these changes are

$$\Delta\tau = K_s\delta, \qquad \Delta\sigma_n = K_n\delta, \tag{5}$$

where K_s and K_n contain interactions within and between faults and compression is positive. A shear-stress increase in the preferred slip direction promotes motion on a receiving fault. A positive normal-stress change increases clamping unless it is accompanied by a compensating pore-pressure increase. Keeping these two stress components separate is essential for interpreting rupture transfer to Fault 3. The interaction matrices are evaluated with a Galerkin boundary-element method and are independently benchmarked in figs. S2–S4.

Hydraulic transport and undrained fault-zone poroelastic response

The model represents two distinct fault-zone effects. The high-diffusivity corridors in the hydraulic grid represent preferential pressure transport through fracture-rich rock over years of injection (26; Figure 2A). A separate parameter represents the undrained pore-pressure response of fault-zone material during slip. The first property controls how injection pressure reaches the faults. The second controls how much of the slip-induced normal-stress change is buffered in effective normal stress. These properties are varied independently in the experiments below.

The elastic interaction kernels K_s and K_n are calculated for a homogeneous elastic medium. Following the undrained fault-zone response described by Cocco and Rice (*27*), we relate slip-induced normal-stress changes to pore-pressure changes. The parameter β_{eff} denotes the fraction of the slip-induced total normal-stress change offset by this pore-pressure response in effective normal stress. We write

$$\Delta P_{\text{slip}} = \widehat{B}\,\Delta\sigma_{n,\text{slip}}, \qquad \beta_{\text{eff}} = \alpha\widehat{B}, \tag{6}$$

where ΔP_{slip} is the pore-pressure change induced by slip-mediated normal-stress transfer, $\Delta\sigma_{n,\text{slip}} = K_n\delta$, and $\widehat{B}$ is the dimensionless pore-pressure response coefficient. The effective-pressure coefficient in the fault calculation is $\alpha = 1$, distinct from the hydraulic-model Biot coefficient α_h. The resulting effective normal stress is

$$\sigma'_n = \sigma_{n,0} - \alpha(P_0 + P_{\text{inj}}) + (1 - \beta_{\text{eff}})K_n\delta. \tag{7}$$

When $\beta_{\text{eff}} = 0$, the slip-induced total normal-stress change contributes fully to effective normal stress, without buffering by undrained pore-pressure feedback. When $\beta_{\text{eff}} = 1$, the pore-pressure response fully offsets the contribution of the slip-induced total normal-stress change $K_n\delta$ to effective normal stress. This feedback does not alter the shear-stress transfer $K_s\delta$. Subsequent diffusion or relaxation of the slip-induced pore-pressure change is not modeled.

Reduced stiffness and a strong stiffness contrast with the host rock can increase this local pore-pressure response. Here, G_f and G_h denote the fault-zone and host-rock shear moduli, respectively. For comparable fault-zone and host-rock densities, $G_f/G_h \approx (V_{S,f}/V_{S,h})^2$. In the isotropic proportional-modulus mapping used below, both drained fault-zone Lamé parameters are scaled by the common ratio G_f/G_h relative to their host-rock values. We map these illustrative fault-zone material properties to β_{eff} using the general poroelastic relation of Cocco and Rice (*27*). The material-property mapping and assumptions underlying this effective representation are provided in the supplementary Materials and Methods (*24*).

Prestress initialization and controlled experiments

We generate fault prestress by evolving each network through repeated earthquake cycles without injection under a prescribed regional loading pattern. The adopted $S_{H\,\max}$ azimuth of 73° lies within the 95% bootstrap confidence region of the regional stress inversion by Sumy et al. (*18*) and is compatible with the modeled slip directions of all three primary faults. We derive the relative distribution of loading velocities V_L by resolving a stress-rate tensor with the same principal directions and principal-stress ratio as the background stress onto each fault. We select a heterogeneous prestress template in which Faults 1–3 have advanced into the later portions of their cycles, then adjust the shear stress uniformly on each of these faults to reproduce the Prague sequence while preserving the inherited along-fault heterogeneity. For the reference simulation, the adjusted shear stress on each fault element remains between the minimum and maximum values reached during the simulated earthquake cycles. Once the prestress is established and injection begins, we set the loading velocity to $V_L = 0$. The loading formulation, evolution durations, selected model states, and stress adjustments are documented in the supplementary Materials and Methods (*24*).

The Figure 2 simulation provides the reference configuration, with $\beta_{\text{eff}} = 1$. In Figures 3A–C, we vary β_{eff} and independently optimize the three fault-wide prestress offsets at each value, while keeping all other model properties fixed. The selection considers the time to rupture initiation on Fault 1, both interevent intervals, and the Fault 3 response, evaluated from its approximate magnitude and maximum slip rate. The hydraulic and operational experiments in Figs. 3D and 4 retain the reference mechanical parameters and prestress. In Figure 5, a common prestress offset is applied to Faults 4–27 relative to their individual long-term mean shear stresses, while fault-wide adjustments to Faults 1–3 preserve the primary Prague sequence. Faults are classified as dynamically rupturing when their maximum slip rate reaches 10^{-2} m s^{-1}. Detailed optimization criteria, parameter grids, operational schedules, and numerical settings are reported in the supplementary Materials and Methods (*24*).

Results

Model for the complete Prague earthquake sequence

In the reference simulation, which uses the initialized prestress state and $\beta_{\text{eff}} = 1$, the modeled pressure perturbation migrated preferentially along the high-diffusivity fault network rather than expanding as a radially symmetric front (Figure 2A).

Within this prestressed system, injection progressively reduced effective normal stress on the three primary faults, with the largest reduction occurring on Fault 1 near the injection source (Figure 2B). The injection-induced pressure perturbation brought Fault 1 to dynamic rupture at 17.96 years. Injection therefore advanced an already highly stressed Fault 1 to failure.

The modeled event timing, magnitudes, and rupture extents agree with independent observational estimates (Figure 2C). Fault 2 ruptured dynamically 0.96 days after Fault 1, consistent with the observed interevent time of 0.86 days, and Fault 3 ruptured 1.95 days after Fault 2, matching the observed interval of approximately 1.95 days (*18*). Assuming a seismogenic width of 3.5 km, the modeled moment magnitudes of Faults 1–3 are M_w 4.9, 5.7, and 4.8, respectively, consistent with the Global Centroid Moment Tensor estimates reported by Keranen et al. (*17*) and the USGS estimates reported by Cochran et al. (*22*). The dynamically rupturing lengths, defined by fault elements reaching $V \geq 10^{-2}$ m/s during each primary event, are 3.91, 14.75, and 2.39 km for Faults 1–3, respectively, close to the corresponding aftershock-covered extents of approximately 4.4, 14.9, and 3.5 km, estimated here from the published aftershock map of Keranen et al. (*17*). The corresponding spatiotemporal slip-rate evolution of the three modeled events is shown in fig. S5 and movie S1. Overall, the model simultaneously reproduces the rupture order, interevent timing, magnitudes, and spatial extents of the Prague sequence.

The modeled stress evolution resolves distinct fault-to-fault triggering mechanisms within the sequence. Fault 1 rupture increases shear stress over part of Fault 2 and triggers its rupture (Figure 2D). Rupture of Fault 2 then imposes competing mechanical effects on Fault 3. It increases shear stress in the modeled slip direction of Fault 3, promoting slip, while simultaneously increasing compressive total normal stress across Fault 3, clamping the fault and inhibiting slip (fig. S6). The local fault-zone pore-pressure response offsets the fraction β_{eff} of this normal-stress increase without altering the shear-stress transfer. When $\beta_{\text{eff}} = 0$, the slip-induced total normal-stress increase is fully expressed as effective-normal-stress clamping. When $\beta_{\text{eff}} = 1$, the local pore-pressure response completely offsets this clamping contribution (fig. S6). At low β_{eff}, the remaining effective-normal-stress clamping prevents the transferred shear loading from developing into dynamic rupture. At sufficiently high β_{eff}, enough of this clamping is buffered for the favorable shear loading from Fault 2 to trigger dynamic rupture of Fault 3 (Figures 2D, 3A–C, and S6).

Figure 2 captures two stages of the Prague sequence. Injection and pressure diffusion prepare Fault 1 for rupture over nearly 18 years, whereas earthquake-driven stress transfer propagates the sequence across faults over the following days. The reproduced sequence provides the reference state for the experiments that follow.

Rupture transfer to Fault 3 by undrained poroelastic feedback

The parameter β_{eff} quantifies the fraction of the slip-induced normal-stress change offset by the local fault-zone pore-pressure response. We varied β_{eff} and independently optimized the three fault-wide prestress offsets at each value using the sequence timing and Fault 3 rupture criteria defined above. Apart from β_{eff} and these prestress adjustments, all hydraulic, frictional, injection, and other mechanical parameters retained their Figure 2 reference values. Event 2 transferred shear stress that promoted slip in the modeled slip direction of Fault 3 (Figure 2D). This favorable shear-stress transfer is unchanged by β_{eff}, which modifies only the slip-induced normal-stress contribution. As β_{eff} increases, the local pore-pressure response offsets a larger fraction of the normal-stress increase, reducing the effective-normal-stress clamping on Fault 3 (fig. S6). Under these controlled comparisons, the best-matching Fault 3 response changes from negligible motion to slow slip and then dynamic rupture (Figures 3A–C).

Among the best-matching simulations, the maximum Fault 3 slip rate crossed 10^{-2} m s^{-1} between the sampled values $\beta_{\mathrm{eff}} = 0.65$ and 0.75 (Figure 3A). Among the dynamically rupturing cases, the modeled Fault 3 magnitude increased from approximately $M_w = 4.4$ toward the observed $M_w = 4.8$ as β_{eff} approached 1 (Figure 3B). Cocco and Rice (*27*) showed that an isotropic fault zone approaches the fault-normal-stress-dominated undrained limit when its shear modulus is much smaller than that of the host rock ($G_f/G_h \ll 1$). To relate this response transition to fault-zone properties, we applied the material-property mapping described in Model and Experimental Design and the supplementary Materials and Methods (*24*). An illustrative end member with $G_f/G_h = 0.1$, implemented by setting both drained Lamé parameters to one-tenth of their corresponding host-rock values, gives $\beta_{\mathrm{eff}} \approx 0.88$ using the reference grain, fluid, and porosity properties. This value falls within the β_{eff} range that produced dynamic rupture of Fault 3 in the best-matching simulations.

Changing β_{eff} has little effect on the Fault 1–Fault 2 interval, which remains close to one day, but strongly changes the timing and character of the Fault 3 response (Figure 3C). Depending on β_{eff}, Fault 3 shows no distinct slip response, undergoes delayed slow slip that remains below the dynamic-rupture threshold, or ruptures dynamically about two days after

Fault 2. Thus, β_{eff} controls whether Fault 3 remains largely inactive, responds through slow slip, or joins the cascade through dynamic rupture.

To isolate hydraulic controls, we held the mechanical, frictional, prestress, and injection parameters of the Figure 2 reference simulation fixed while varying the host-rock and damage-zone diffusivities. These experiments produced times to rupture initiation ranging from a few years to more than a century and changed which fault ruptured first across the parameter space (Figure 3D). All tested diffusivity combinations ultimately produced dynamic rupture on the three primary faults. Within this fixed mechanical and prestress configuration, hydraulic diffusivity therefore controls the timing and location of rupture initiation, whereas effective fault-zone poroelastic coupling governs whether Fault 3 participates dynamically in the cascade.

Well placement and operational earthquake mitigation strategies

Well location and injection history are operational variables that can be modified directly. We used the Figure 2 reference model that reproduces the Prague sequence as the common baseline for controlled experiments, retaining the reference configuration except for the operational variable being tested. We examined whether changing source–fault separation or the injection time function can postpone earthquake initiation and increase the cumulative fluid input delivered before instability. To evaluate source–fault separation at a fixed injection rate, we continued injection until the first rupture in one suite and applied a common 18-year injection schedule followed, where necessary, by post-shut-in evolution to the first rupture in the other (Figure 4A).

With injection maintained at the same rate until rupture began on a fault, increasing the source–fault distance from approximately 0.07 to 9.15 km delayed the first rupture from approximately 16 to 242 years, substantially increasing both the injection duration and cumulative volume delivered before instability. Under the common 18-year schedule, nearby sources produced rupture during injection or shortly after shut-in, whereas rupture began progressively later after shut-in as source–fault separation increased. At the largest distance, rupture began at approximately 260 years, close to the 276-year no-injection control. This control represents the internal evolution of the initialized prestressed system with $q_{2\text{D}} = 0$

and $V_L = 0$, rather than an estimate of the natural recurrence time of the Prague sequence. Together, these experiments show that greater source–fault separation weakens hydraulic loading and delays rupture initiation under both continuous and finite-duration injection. The distance effect is more pronounced under the fixed-duration schedule because the injected volume is held constant, whereas in the continuous-to-failure experiment the longer time to rupture initiation allows more fluid to be injected, partly compensating for the weaker hydraulic influence at greater distance. At the largest tested distance, the finite injection episode produced only a limited advance of failure, highlighting the importance of well–fault separation for induced-seismicity mitigation.

At a fixed source location, injection history controlled rupture initiation primarily through the effective injection rate (Figures 4B–D). Under steady injection, increasing the imposed two-dimensional rate from 0.03 to 30 times the reference rate $q_{\mathrm{ref}} \approx 1.7 \times 10^{-7}\ \mathrm{m}^2\,\mathrm{s}^{-1}$ shortened the time to rupture initiation from approximately 198 years to 0.23 years. When injection rates were high enough for hydraulic forcing to dominate the approach to failure, time to rupture initiation scaled approximately inversely with injection rate. As the injection rate decreased and hydraulic forcing weakened relative to the fault system's internal evolution, times to rupture initiation converged toward the no-injection control (Figure 4B). Increasing the shut-in interval delayed rupture initiation when the peak injection rate was fixed, but rupture initiation remained near 18 years when the cycle-averaged rate was preserved (Figure 4C). Extraction similarly delayed rupture initiation, reaching approximately 178 years at the largest tested extraction-to-injection ratio and approximately following the inverse net injection rate (Figure 4D). Together, Figures 4B–D show that, when hydraulic forcing dominates the approach to failure and source location is fixed, steady, intermittent, and injection–extraction schedules produce rupture after broadly similar cumulative net fluid input. Thus, for a given cumulative net fluid input, reducing the effective injection rate and increasing well–fault separation provide complementary means of delaying rupture initiation.

Role of prestress and fault interactions

To examine how receiver-fault prestress and network interactions shape activation beyond the primary Prague sequence, we preserved the reproduced sequence while applying a common prestress offset to receiver Faults 4–27 relative to their individual long-term mean shear stresses, without altering their inherited along-fault stress heterogeneity (Figure 5 and movie S2).

At the end of the modeled Prague sequence, slip-mediated shear-stress changes were spatially heterogeneous and included both promoting and inhibiting regions (Figure 5A, main panel). The effective-normal-stress changes at sequence end were evaluated relative to the injection-onset state and included hydraulic loading and slip-mediated poroelastic feedback (Figure 5A, inset).

Receiver-fault responses were evaluated from the end of the modeled Prague sequence to model year 100. None of Faults 1–3 underwent a subsequent dynamic rupture during this interval in any analyzed simulation. Over the tested receiver-fault prestress offsets of 0–0.5 MPa, increasing the offset enhanced the overall response, but only a few receiver faults ruptured dynamically. The experiments showed a marked transition near a +0.3 MPa prestress offset: none of Faults 4–27 ruptured dynamically at lower offsets, whereas Faults 5 and 6 reached the largest post-sequence velocities and ruptured dynamically at offsets of +0.3 MPa and above (Figure 5B, upper panel). Their preferential responses were consistent with positive slip-mediated shear-stress changes over much of both faults at sequence end (Figure 5A). Faults 5 and 6 ruptured dynamically within five years of sequence end (Figure 5B, lower panels). The combined scalar moments of Faults 5 and 6 corresponded to $M_w = 4.8$, 4.9, and 5.0 at prestress offsets of +0.3, +0.4, and +0.5 MPa, respectively. The magnitude of the combined rupture therefore increased with the receiver-fault prestress offset.

Prestress is a first-order control on fault activation, but its absolute value could not be constrained precisely from the available observations. These experiments therefore target relative fault susceptibility rather than unique fault-specific failure thresholds. Applying the same prestress offset relative to the long-term mean of each fault allowed us to identify which faults remained preferentially activated as the network was brought progressively closer to failure. The strongly nonuniform response to the same prestress offset demonstrates the important roles of fault orientation, position relative to the primary ruptures, and signed elastic interactions. The transition near +0.3 MPa and the elevated responses of Faults 5 and 6 are specific to the present Prague network and parameterization. The broader result is that fault-specific relative susceptibility can be identified even when absolute prestress remains uncertain.

Discussion

Poroelastic feedback in fault damage zones

The Prague simulations distinguish two roles of fault damage zones in sequence evolution. Fault-zone poroelastic feedback governs rupture transfer to Fault 3, whereas preferential pore-pressure transmission along high-diffusivity fault zones shapes the long-term hydraulic preparation for rupture (Figure 3).

Reproducing the third Prague event provides the critical test for whether a dynamic model can transfer rupture to a mechanically less favorable fault. Static stress-change calculations by Sumy et al. (*18*) did not show that the first two events favored its occurrence, and previous physics-based network modeling reproduced the first two events but not the third (*23*). Across the prestress-adjusted β_{eff} experiments, the best-matching Fault 3 response changes from negligible motion to slow slip and then dynamic rupture as β_{eff} increases (Figures 3A–C). Event 2 supplies favorable shear loading, but dynamic rupture occurs only when fault-zone poroelastic feedback offsets enough of the opposing effective normal stress clamping. This feedback does not alter the shear-stress transfer (Figures 2D, 3A–C, and S6).

Cocco and Rice (*27*) showed that an isotropic fault zone with a shear modulus much smaller than that of the surrounding host rock can develop an undrained pore-pressure response dominated by fault-normal stress, reducing the effective normal stress clamping produced by compression. By embedding this response within an evolving frictional fault system, our simulations show how it determines whether favorable shear loading develops into rupture transfer (Figures 3A–C). Published seismological estimates and compilations of fault-zone velocity reductions, together with geodetic constraints on damage-zone shear modulus, imply $G_f/G_h \approx 0.1$–0.6 under the density and proportional-modulus assumptions used here (*28–32*). This range corresponds to $\beta_{\text{eff}} \approx 0.44$–$0.88$ and includes the feedback strength required for dynamic Fault 3 rupture, which lies between the tested values $\beta_{\text{eff}} = 0.65$

and 0.75.

Injection-induced pore pressure changes fault strength, while slip-induced normal-stress changes feed back on fault-zone pore pressure and subsequent slip. Our formulation represents this two-way hydromechanical coupling through an undrained fault-zone response, at nearly the same computational cost as a one-way calculation in which injection pressure affects fault slip without slip-induced pore-pressure feedback. This efficiency facilitates exploration of how hydraulic conditions and fault-network properties jointly shape earthquake sequences.

Hydraulically, the Figure 3D experiments represent fault damage zones as corridors with enhanced diffusivity compared to that of the surrounding host rock. Varying the fault-zone and host-rock diffusivities affects when rupture begins and which fault ruptures first under a fixed mechanical and prestress configuration (Figure 3D). Comparable preferential pathways have been inferred in other induced-seismicity sequences. Peña Castro et al. (*33*) proposed rapid pressure transmission from hydraulic-fracturing wells to a basement fault through a high-permeability conduit and fault damage zone in the Montney region of British Columbia, Canada. Near Peace River, Alberta, Canada, Schultz et al. (*34*) inferred pressure buildup in a permeable basal aquifer followed by downward migration along a basement-rooted fault damage zone, whereas at Weiyuan in the southwestern Sichuan Basin, China, Sheng et al. (*35*) attributed diffusion-like seismicity migration and high inferred effective diffusivities to preferential transport along reactivated faults. These field interpretations provide natural analogues for the fault-controlled pressure pathways represented by the modeled diffusivity contrast.

The experiments in Figure 3D prescribe fixed fault-zone and host-rock diffusivities, whereas natural fault-zone permeability can evolve during and after slip (*36*). Dilation, compaction, coseismic damage, and subsequent sealing can produce fault-valve behavior, and rupture-induced permeability enhancement has been proposed as a contributor to induced-earthquake cascades (*37–39*). Such permeability evolution would extend the preferential pressure-transmission role considered here by allowing rupture to modify subsequent fluid pathways. It is physically distinct from the rapid poroelastic feedback represented by β_{eff}.

From injection-induced rupture initiation to fault-network escalation

Previous studies have identified an anthropogenic perturbation, a pre-existing fault capable of hosting the event, and a hydraulic or mechanical pathway linking the perturbation to the fault as the principal factors for consequential induced seismicity (*1, 3, 11, 40*). Yet, how these mechanisms interact remains incompletely understood, including why similar injection operations differ in whether, when, and where earthquakes begin (*2*); why injected volume does not uniquely determine maximum magnitude (*41*); and why some induced ruptures remain bounded while others develop into multi-fault cascades (*9, 13*). By resolving hydraulic preparation, multi-fault rupture transfer, and post-sequence network response within a single observation-constrained Prague sequence, our simulations provide a consistent framework for addressing these questions.

The simulations first help explain why similar injection operations can produce different seismic responses, including whether, when, and where earthquakes begin. Site comparisons have long emphasized the combined importance of hydraulic access, basement and fault architecture, and proximity to failure (*2, 11, 42*). Our simulations provide a dynamic interpretation. The initial stability margin sets the additional loading required for instability, whereas injection history and hydraulic connectivity determine where and how rapidly that loading is supplied, producing an approximately 18-year hydraulic preparation before Fault 1 rupture (Figure 2B). The sequence near Peace River, Alberta, Canada, shows a comparable multiyear progression. Southern-cluster seismicity emerged several years after wastewater disposal began and culminated in the 2022 M_w5.1 earthquake about a decade after operations started (*34*). Schultz et al. (*34*) attributed this evolution primarily to pressure buildup in a basal aquifer and subsequent migration along a basement-rooted fault pathway until critical slip conditions were reached. This progression from pressure transmission to instability of a prestressed fault is resolved dynamically in our Prague simulations, providing a transferable physical framework for understanding induced earthquakes that occur years after injection begins.

Our model also clarifies why injected volume does not uniquely determine the maximum magnitude of induced earthquakes. The distinction between anthropogenic triggering and the release of pre-existing tectonic strain energy is well established (*1–3, 40, 43, 44*). Our contribution is to resolve this transition dynamically within the complete Prague sequence. Injection-induced pore-pressure diffusion brings Fault 1 to rupture (Figure 2B), but the subsequent mainshock and third event emerge through stress transfer and frictional evolution within the prestressed fault system (Figure 2D). Once rupture begins, its eventual size depends increasingly on the stored stress and the dimensions of fault structure available for rupture growth. Regional fault mapping and stress analysis support this interpretation: the mapped faults hosting the Prague, Pawnee, and Cushing $M \geq 5$ earthquakes were inferred to be critically oriented in the local stress field, and maximum magnitude increased with mapped fault length across the regional fault population (*45*). Injection rate and volume can therefore influence when instability begins without uniquely specifying how far the resulting rupture will propagate or how large it will become. Physically based maximum-magnitude assessments must consequently consider fault prestress and connected fault structure in addition to the imposed hydraulic perturbation.

A third implication concerns why some induced ruptures remain bounded whereas others escalate across multiple faults. The Prague simulations resolve escalation at two nested scales. The primary sequence develops through rupture transfer across Faults 1–3 (Figures 2 and 3). The post-sequence fault-network experiments show that surrounding-fault prestress governs whether dynamic rupture occurs beyond the primary sequence, while fault geometry and signed elastic interactions shape which surrounding faults rupture (Figure 5). On a single fault, prestress, frictional conditions, and fault dimensions govern whether a hydraulically initiated rupture arrests or runs away (*13, 46*). The Prague simulations extend this arrested–runaway problem to an interacting fault network. Global sequence statistics and numerical simulations further indicate that structural complexity can promote rupture arrest as well as rupture transfer (*47–49*). Together, these results identify the state and structure of the surrounding fault system as controls on whether a hydraulically initiated rupture remains bounded or escalates.

Implications for operational mitigation

Operational mitigation can alter both the effective injection rate and hydraulic access to the fault network. Well placement and injection history are actionable even when absolute fault prestress remains difficult to constrain. At a fixed source location, the steady, intermittent, and injection–extraction experiments show that rupture initiation timing depends primarily on the time-averaged or net injection rate when hydraulic forcing dominates the approach to failure (Figures 4B–D). Intermittency or extraction therefore delays rupture initiation only insofar as it reduces the effective injection rate in these experiments. Their additional field-scale effects will depend on source–sink geometry and site-specific hydraulic and geomechanical responses.

Greater source–fault separation substantially delays earthquake initiation under both continuous and finite-duration injection. When injection continues until rupture begins, this delay expands the operational window and allows greater cumulative fluid input before instability (Figure 4A). Where fault geometry and hydraulic connectivity are sufficiently resolved, this result supports pre-operational well placement that prioritizes separation from basement faults and avoidance of susceptible structures (*2–4, 11, 42, 50*).

In February 2024, an $M_w5.1$ earthquake occurred in the Prague area, approximately 12 years after the 2011 sequence. The Oklahoma Geological Survey location places the epicenter near modeled Faults 1, 2, 10, and 17, whereas the USGS location places it closer to Faults 15 and 16 (*51, 52*). The simulations in Figure 5 did not produce a corresponding dynamic rupture near either reported location within the tested receiver-fault prestress range. However, the modeled 2011 sequence increased shear stress on parts of Faults 15 and 16, while injection-induced pore pressure reduced effective normal stress in this area (Figure 5A), both of which would favor subsequent instability. Initial shear stresses on nearby receiver faults may have exceeded their respective long-term means by more than the maximum offset of +0.5 MPa explored here, and additional injection at nearby wells may have provided hydraulic loading beyond that represented in the model. Higher fault-specific prestress and additional hydraulic loading are therefore two plausible explanations for later rupture in this region.

Together, the operational experiments in Figure 4 and the post-sequence fault-network experiments in Figure 5 indicate that hazard assessment should evolve as an induced sequence develops. Before significant rupture, operational measurements, pressure estimates, and seismicity trends provide the most direct constraints on the approach to instability, and changes in injection or extraction can modify the rate of further hydraulic loading. Once a significant dynamic event begins to redistribute stress through the fault network, hazard assessment should expand to include fault geometry, connectivity, plausible prestress states, and elastic interactions while continuing to track hydraulic forcing. Conventional traffic-light systems respond to prescribed magnitude or ground-motion thresholds, whereas adaptive approaches update probabilistic forecasts as hydraulic and seismic observations accumulate (*4, 53, 54*). Our results suggest that such updates should encompass both the estimated level of risk and the physical scope of the hazard model, expanding beyond primarily hydraulic indicators to include the state and interaction potential of the surrounding fault network. Evidence that large events can occur after shut-in and that earthquake-mediated stress interactions can enhance post-injection seismicity supports this broader assessment (*3, 40, 50, 55, 56*). Because the onset of fault-to-fault interaction depends on site-specific fault geometry and stress state, the threshold for expanding the hazard model should be defined locally rather than by a universal magnitude or pressure value.

Within a single computational framework, the model connects long-term injection to rupture initiation, reproduces the complete Prague cascade, quantifies operational controls on rupture initiation, and tests the response of a broader prestressed network (Figures 2–5). The Prague sequence provides an observational benchmark for resolving these processes dynamically. Within this sequence, undrained fault-zone poroelastic feedback enables rupture transfer to Fault 3, providing the key mechanistic link between injection-triggered rupture initiation and multi-fault rupture (Figures 2 and 3). More broadly, the study shifts the modeling emphasis from earthquake initiation alone toward determining when initiated slip remains bounded and when it mobilizes a larger interacting fault system.

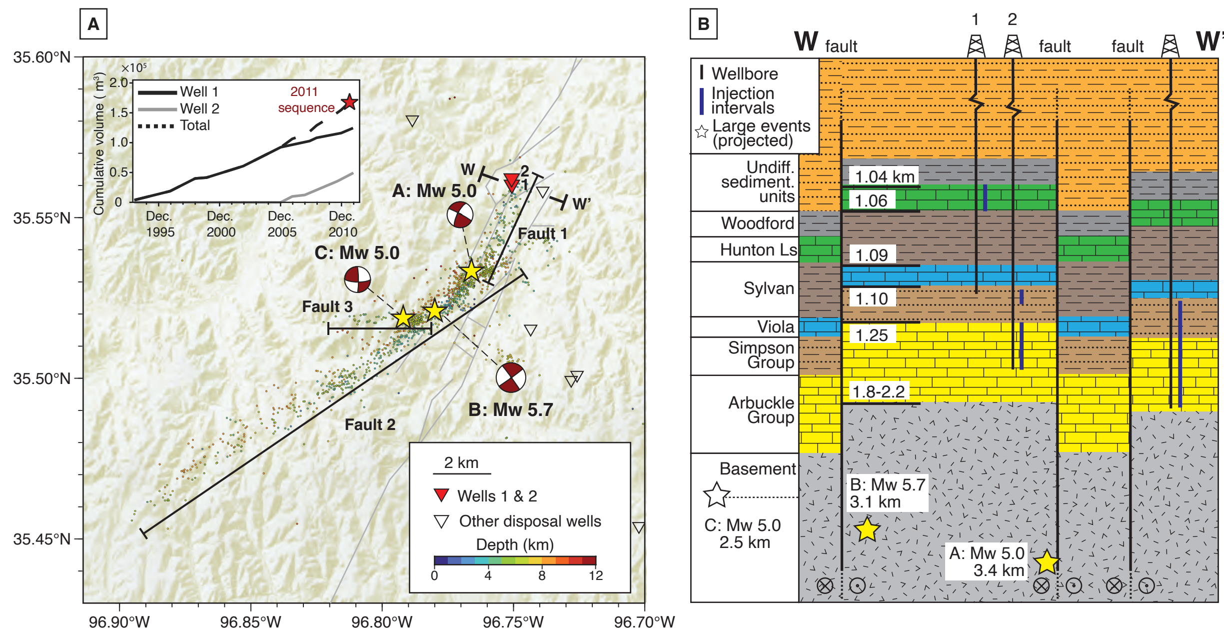

Figure 1: **Observational setting of the 2011 Prague earthquake sequence.** (**A**) Map of the Wilzetta fault system showing disposal wells, relocated seismicity, focal mechanisms, modeled Faults 1–3, and the three large earthquakes. The shaded-relief background is derived from the U.S. Geological Survey 3D Elevation Program 1/3-arc-second digital elevation model. The inset shows cumulative injection volumes for Wells 1 and 2 and their combined total. Wilzetta fault traces are based on Way (*19*), relocated seismicity is from McNamara et al. (*20*), focal mechanisms are from Sumy et al. (*18*), and well locations and injection histories are from Keranen et al. (*17*). Earthquake colors indicate depth. (**B**) Geological cross section W–W′ showing stratigraphy, faults, wellbores and injection intervals, and the projected locations of the three large events relative to the sedimentary section and crystalline basement. The cross section is schematic. Formation-top and well depths are referenced to sea level following Keranen et al. (*17*). The cross section is compiled from Keranen et al. (*17*) and Sumy et al. (*18*).

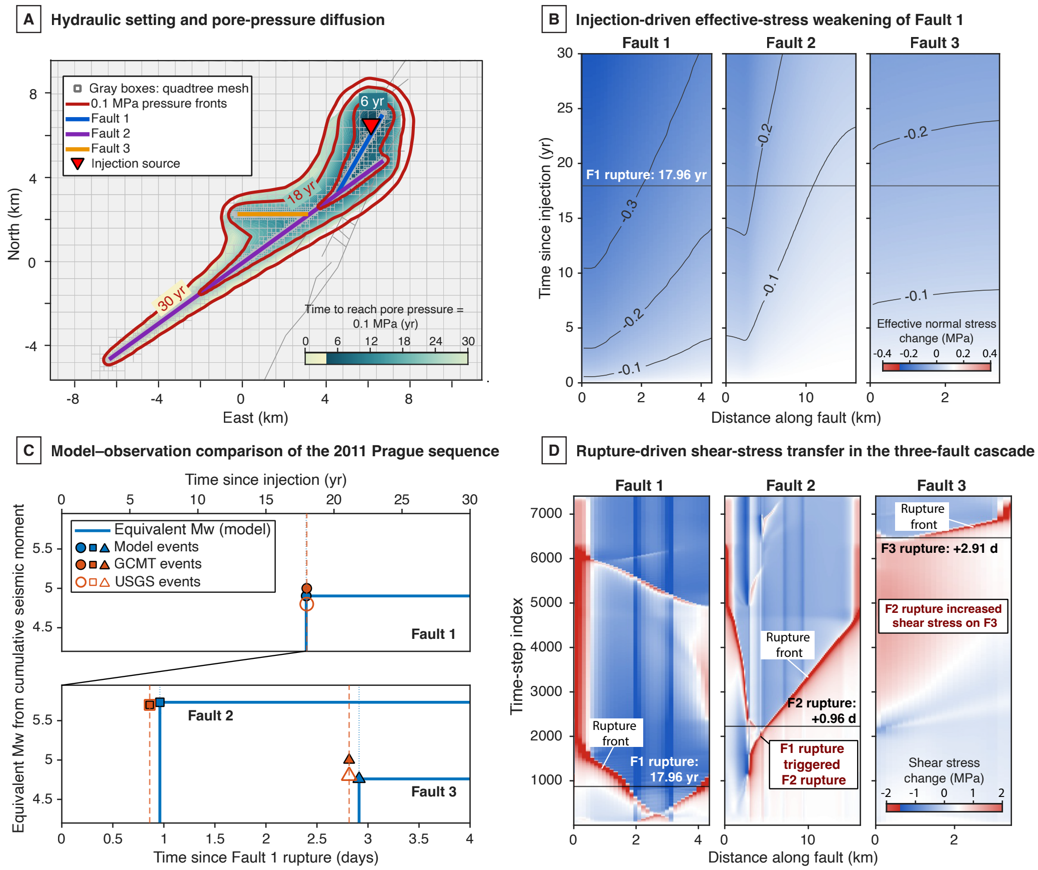

Figure 2: **Hydraulic weakening and rupture-driven stress transfer reproduce the 2011 Prague sequence.** (**A**) Adaptive quadtree grid, modeled Faults 1–3, injection source, and arrival of the 0.1-MPa pore-pressure front. Contours show the front positions at 6, 18, and 30 years. (**B**) Injection-induced effective-normal-stress changes along Faults 1–3 relative to their values at injection onset. Negative values indicate unclamping under the compression-positive convention, and the horizontal line marks Fault 1 rupture at 17.96 years. (**C**) Model–observation comparison of event timing and magnitude. The blue curve shows the equivalent moment magnitude of the cumulative modeled seismic moment, while symbols mark individual modeled, GCMT, and USGS events. The upper panel spans the injection period, and the lower panel expands the first four days after Fault 1 rupture. Observed event timing is from Sumy et al. (*18*), GCMT magnitudes are reported by Keranen et al. (*17*), and USGS magnitudes are reported by Cochran et al. (*22*). (**D**) Slip-mediated shear-stress changes relative to their values at injection onset during the three-fault cascade. The vertical coordinate indexes successive adaptive numerical time steps used to resolve the rapid rupture sequence. The steps are not uniformly spaced in physical time, and the corresponding rupture times are annotated.

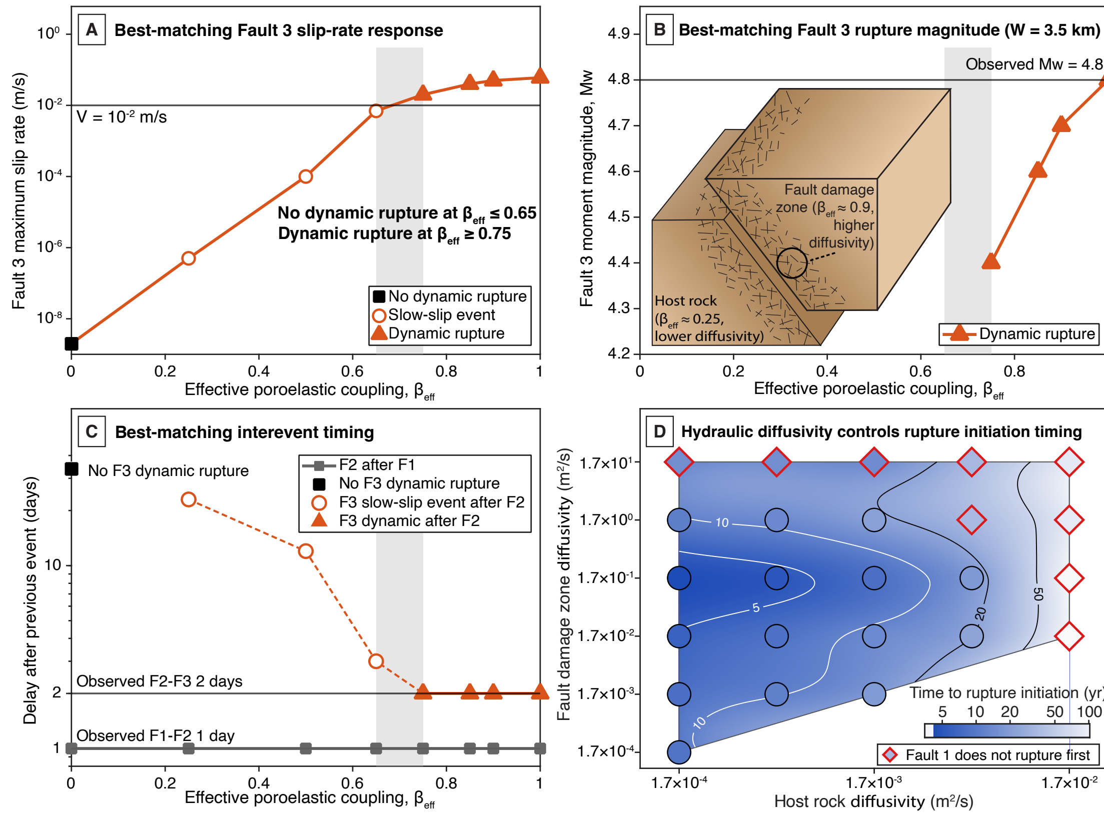

Figure 3: **Effective fault-zone poroelastic feedback and hydraulic properties control different stages of the sequence.** Panels (**A**)–(**C**) show the best-matching prestress-adjusted simulation for each β_{eff}, defined as the fraction of slip-mediated normal-stress transfer buffered by fault-zone pore-pressure response. $\beta_{\text{eff}} = 0$ is the one-way-coupling limit. (**A**) Maximum Fault 3 slip rate versus β_{eff}. The horizontal line marks $V = 10^{-2}$ m s^{-1}, used to identify dynamic rupture. Shading brackets the transition to dynamic Fault 3 rupture between the tested values $\beta_{\text{eff}} = 0.65$ and 0.75. (**B**) Fault 3 moment magnitude for dynamic cases, using a seismogenic width $W = 3.5$ km. The horizontal line marks the observed $M_w = 4.8$. The schematic shows contrasts in effective coupling and diffusivity between host rock and the fault damage zone. (**C**) Delay between Events 1 and 2 and between Event 2 and the principal Fault 3 response versus β_{eff}, with slow-slip and dynamic Fault 3 responses distinguished. Observed delays are approximately one and two days. (**D**) Rupture-initiation time across host-rock and fault-damage-zone diffusivities, with all other parameters fixed at their Fig. 2 reference values. Colors and contours show initiation time. Red outlines mark cases in which Fault 1 does not rupture first. Observed timing is from Sumy et al. (*18*), and the observed Fault 3 magnitude is the USGS estimate reported by Cochran et al. (*22*).

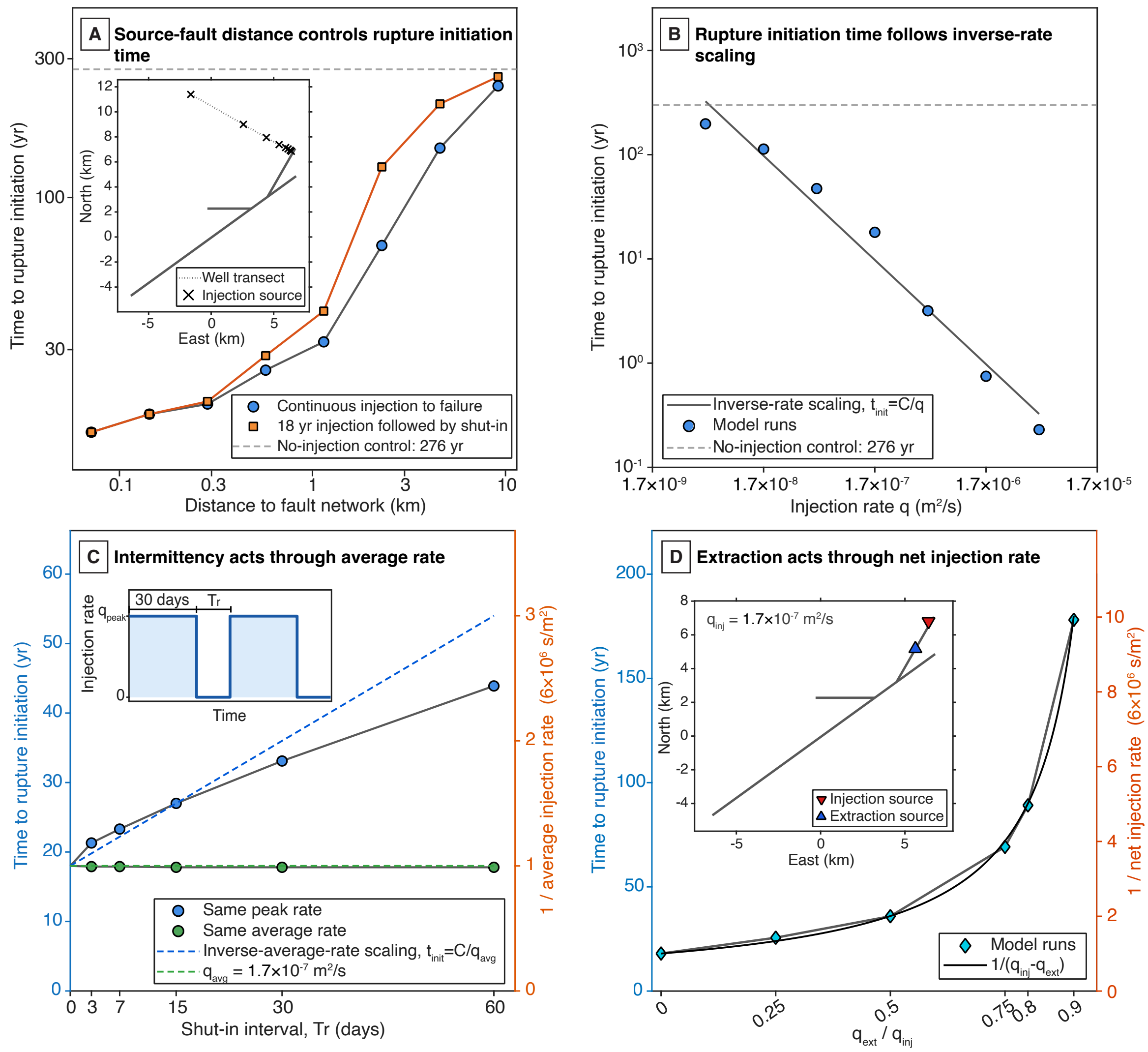

Figure 4: **Operational and geometric controls on rupture initiation timing.** (**A**) Time to rupture initiation as a function of source–fault distance under continuous injection and an 18-year injection schedule followed, where necessary, by post-shut-in evolution to the first rupture. The dashed line marks the 276-year no-injection control, and the inset shows the source transect. (**B**) Time to rupture initiation under steady injection at different two-dimensional source rates, compared with inverse-rate scaling and the no-injection control. (**C**) Intermittent-injection experiments at fixed peak rate and fixed cycle-averaged rate. The inset illustrates the 30-day injection interval and the variable shut-in interval T_r. (**D**) Injection–extraction experiments showing the response to decreasing net injection rate. The inset shows the injection and extraction locations. All experiments began from the same initialized mechanical, frictional, and prestress state. Active long-term loading was absent ($V_L = 0$) throughout the operational and post-shut-in calculations.

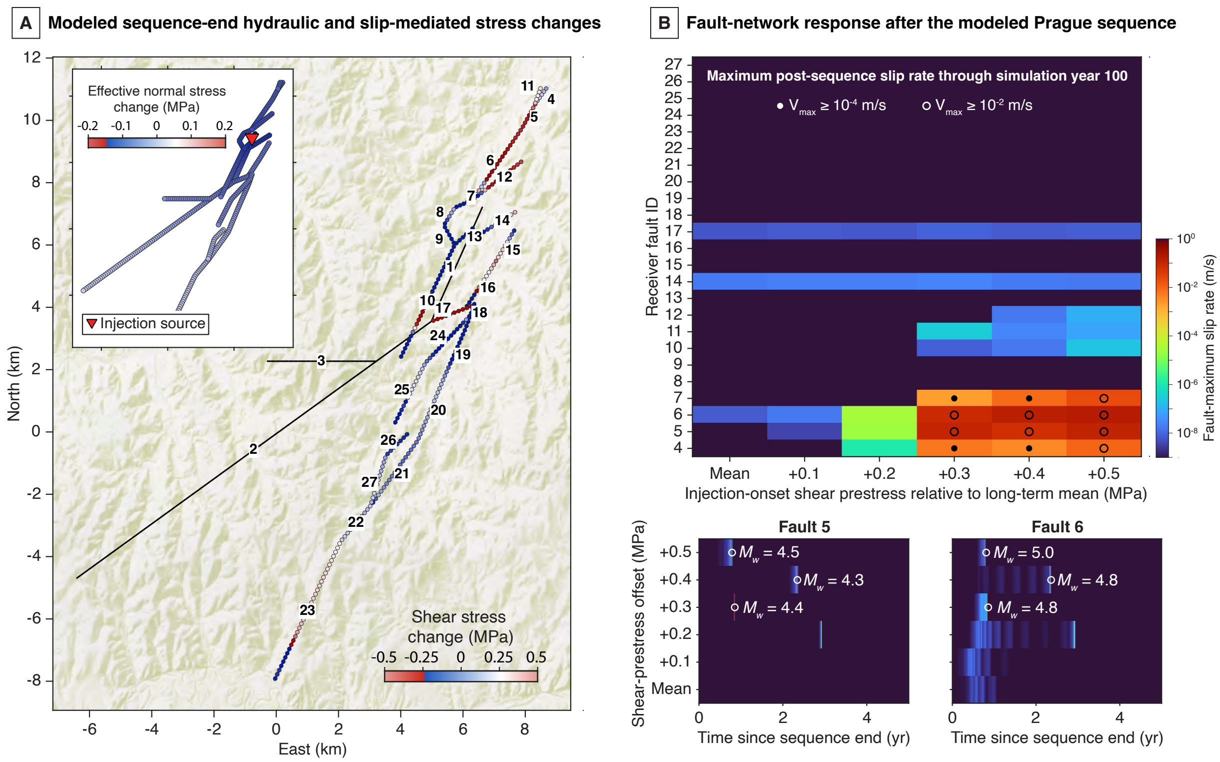

Figure 5: **Conditional fault-network response following the reproduced Prague sequence.** (**A**) Hydraulic and slip-mediated stress changes at sequence end, evaluated relative to the injection-onset state. The main panel shows slip-mediated shear-stress change and fault IDs over a shaded-relief background derived from the U.S. Geological Survey 3D Elevation Program 1/3-arc-second digital elevation model, and the inset shows effective-normal-stress change including hydraulic and slip-mediated contributions. (**B**) Upper panel: fault-maximum post-sequence slip rate, evaluated from sequence end to model year 100 on receiver Faults 4–27 as a function of the receiver-fault prestress offset from the long-term mean shear stress of each fault. Filled and open symbols denote $V_{\max} \geq 10^{-4}$ m s^{-1} and $V_{\max} \geq 10^{-2}$ m s^{-1}, respectively. Lower panels: fault-maximum slip-rate histories during the first five years after sequence end for Faults 5 and 6. Open circles mark the first crossing of the dynamic-rupture threshold. The labeled M_w values are calculated separately from the scalar seismic moment accumulated on each fault during the complete dynamic rupture episode. The combined scalar moments of Faults 5 and 6 correspond to M_w = 4.8, 4.9, and 5.0 at prestress offsets of +0.3, +0.4, and +0.5 MPa, respectively. Every displayed simulation preserves the calibrated injection-to-event timing, interevent delays, rupture order, and modeled magnitudes of the primary Prague sequence.

References and Notes

1. W. L. Ellsworth, Injection-Induced Earthquakes. *Science* **341** (6142), 1225942 (2013), doi:10.1126/science.1225942.

2. K. M. Keranen, M. Weingarten, Induced Seismicity. *Annual Review of Earth and Planetary Sciences* **46** (1), 149–174 (2018), doi:10.1146/annurev-earth-082517-010054.

3. M. J. A. Moein, *et al.*, The Physical Mechanisms of Induced Earthquakes. *Nature Reviews Earth & Environment* **4** (12), 847–863 (2023), doi:10.1038/s43017-023-00497-8.

4. W. Zhou, *et al.*, Managing Induced Seismicity Risks From Enhanced Geothermal Systems: A Good Practice Guideline. *Reviews of Geophysics* **62** (4), e2024RG000849 (2024), doi:10.1029/2024RG000849.

5. P. Segall, S. Lu, Injection-induced seismicity: Poroelastic and earthquake nucleation effects. *Journal of Geophysical Research: Solid Earth* **120** (7), 5082–5103 (2015), doi: 10.1002/2015JB012060.

6. Y. Guglielmi, F. Cappa, J.-P. Avouac, P. Henry, D. Elsworth, Seismicity triggered by fluid injection–induced aseismic slip. *Science* **348** (6240), 1224–1226 (2015), doi:10.1126/science.aab0476.

7. M. R. M. Brown, S. Ge, Small Earthquakes Matter in Injection-Induced Seismicity. *Geophysical Research Letters* **45** (11), 5445–5453 (2018), doi:10.1029/2018GL077472.

8. P. Bhattacharya, R. C. Viesca, Fluid-induced aseismic fault slip outpaces pore-fluid migration. *Science* **364** (6439), 464–468 (2019), doi:10.1126/science.aaw7354.

9. S. Ge, M. O. Saar, Review: Induced Seismicity During Geoenergy Development—A Hydromechanical Perspective. *Journal of Geophysical Research: Solid Earth* **127** (3), e2021JB023141 (2022), doi:10.1029/2021JB023141.

10. N. Berrios-Rivera, S. Ozawa, E. M. Dunham, Fluid Pressure Diffusion and Elastic Stress Transfer From Seismic Slip Control Slip Front Expansion in Fluid-Driven Swarm Seis-

micity. *Journal of Geophysical Research: Solid Earth* **130** (12), e2025JB032438 (2025), doi:10.1029/2025JB032438.

11. R. Schultz, *et al.*, Hydraulic Fracturing-Induced Seismicity. *Reviews of Geophysics* **58** (3), e2019RG000695 (2020), doi:10.1029/2019RG000695.

12. D. I. Garagash, L. N. Germanovich, Nucleation and arrest of dynamic slip on a pressurized fault. *Journal of Geophysical Research: Solid Earth* **117** (B10), B10310 (2012), doi:10.1029/2012JB009209.

13. M. Galis, J. P. Ampuero, P. M. Mai, F. Cappa, Induced Seismicity Provides Insight Into Why Earthquake Ruptures Stop. *Science Advances* **3** (12), eaap7528 (2017), doi: 10.1126/sciadv.aap7528.

14. J. H. Norbeck, R. N. Horne, Evidence for a transient hydromechanical and frictional faulting response during the 2011 M_w 5.6 Prague, Oklahoma earthquake sequence. *Journal of Geophysical Research: Solid Earth* **121** (12), 8688–8705 (2016), doi: 10.1002/2016JB013148.

15. Y. Qin, X. Chen, T. Chen, R. E. Abercrombie, Influence of Fault Architecture on Induced Earthquake Sequence Evolution Revealed by High-Resolution Focal Mechanism Solutions. *Journal of Geophysical Research: Solid Earth* **127** (11), e2022JB025040 (2022), doi:10.1029/2022JB025040.

16. L. Huang, E. R. Heimisson, L. Dal Zilio, Poroelastic effects on rupture propagation across fault stepovers. *Earth and Planetary Science Letters* **649**, 119103 (2025), doi: 10.1016/j.epsl.2024.119103.

17. K. M. Keranen, H. M. Savage, G. A. Abers, E. S. Cochran, Potentially Induced Earthquakes in Oklahoma, USA: Links Between Wastewater Injection and the 2011 M_w 5.7 Earthquake Sequence. *Geology* **41** (6), 699–702 (2013), doi:10.1130/G34045.1.

18. D. F. Sumy, E. S. Cochran, K. M. Keranen, M. Wei, G. A. Abers, Observations of Static Coulomb Stress Triggering of the November 2011 M5.7 Oklahoma Earthquake

Sequence. *Journal of Geophysical Research: Solid Earth* **119** (3), 1904–1923 (2014), doi: 10.1002/2013JB010612.

19. H. S. K. Way, *Structural Study of the Hunton Lime of the Wilzetta Field, T12–13 N, R5E, Lincoln County, Oklahoma, Pertaining to the Exploration for Hydrocarbons*, Master's thesis, Oklahoma State University, Stillwater, Oklahoma (1983), `https://shareok.org/handle/11244/16448`.

20. D. E. McNamara, *et al.*, Earthquake Hypocenters and Focal Mechanisms in Central Oklahoma Reveal a Complex System of Reactivated Subsurface Strike-Slip Faulting. *Geophysical Research Letters* **42** (8), 2742–2749 (2015), doi:10.1002/2014GL062730.

21. N. D. McMahon, R. C. Aster, W. L. Yeck, D. E. McNamara, H. M. Benz, Spatiotemporal Evolution of the 2011 Prague, Oklahoma, Aftershock Sequence Revealed Using Subspace Detection and Relocation. *Geophysical Research Letters* **44** (14), 7149–7158 (2017), doi: 10.1002/2017GL072944.

22. E. S. Cochran, R. J. Skoumal, D. McPhillips, Z. E. Ross, K. M. Keranen, Activation of Optimally and Unfavourably Oriented Faults in a Uniform Local Stress Field During the 2011 Prague, Oklahoma, Sequence. *Geophysical Journal International* **222** (1), 153–168 (2020), doi:10.1093/gji/ggaa153.

23. K. Im, J.-P. Avouac, Quake-DFN: A Software for Simulating Sequences of Induced Earthquakes in a Discrete Fault Network. *Bulletin of the Seismological Society of America* **114** (5), 2341–2358 (2024), doi:10.1785/0120230299.

24. Materials and methods are available as supplementary material.

25. S. Barbot, Modulation of fault strength during the seismic cycle by grain-size evolution around contact junctions. *Tectonophysics* **765**, 129–145 (2019), doi:10.1016/j.tecto.2019.05.004.

26. J. S. Caine, J. P. Evans, C. B. Forster, Fault Zone Architecture and Permeability Structure. *Geology* **24** (11), 1025–1028 (1996), doi:10.1130/0091-7613(1996)024⟨1025:FZAAPS⟩2.3.CO;2.

27. M. Cocco, J. R. Rice, Pore Pressure and Poroelasticity Effects in Coulomb Stress Analysis of Earthquake Interactions. *Journal of Geophysical Research: Solid Earth* **107** (B2), 2030 (2002), doi:10.1029/2000JB000138.

28. S. Barbot, Y. Fialko, D. Sandwell, Three-dimensional models of elastostatic deformation in heterogeneous media, with applications to the Eastern California Shear Zone. *Geophysical Journal International* **179** (1), 500–520 (2009), doi:10.1111/j.1365-246X.2009.04194.x.

29. Y.-G. Li, P. E. Malin, San Andreas Fault Damage at SAFOD Viewed With Fault-Guided Waves. *Geophysical Research Letters* **35** (8), L08304 (2008), doi:10.1029/2007GL032924.

30. M. A. Lewis, Y. Ben-Zion, Diversity of Fault Zone Damage and Trapping Structures in the Parkfield Section of the San Andreas Fault From Comprehensive Analysis of Near Fault Seismograms. *Geophysical Journal International* **183** (3), 1579–1595 (2010), doi:10.1111/j.1365-246X.2010.04816.x.

31. Y. Huang, J.-P. Ampuero, D. V. Helmberger, Earthquake Ruptures Modulated by Waves in Damaged Fault Zones. *Journal of Geophysical Research: Solid Earth* **119** (4), 3133–3154 (2014), doi:10.1002/2013JB010724.

32. C. Li, Z. Ma, X. Xi, G. Zhang, X. Shan, Constraining Shear Strength of Fault Damage Zone Using Geodetic Data and Numerical Simulation. *Geophysical Research Letters* **51** (10), e2024GL108169 (2024), doi:10.1029/2024GL108169.

33. A. F. Peña Castro, *et al.*, Stress Chatter via Fluid Flow and Fault Slip in a Hydraulic Fracturing-Induced Earthquake Sequence in the Montney Formation, British Columbia. *Geophysical Research Letters* **47** (14), e2020GL087254 (2020), doi:10.1029/2020GL087254.

34. R. Schultz, *et al.*, Disposal From In Situ Bitumen Recovery Induced the M_L 5.6 Peace River Earthquake. *Geophysical Research Letters* **50** (6), e2023GL102940 (2023), doi:10.1029/2023GL102940.

35. M. Sheng, *et al.*, Earthquakes Triggered by Fluid Diffusion and Boosted by Fault Reactivation in Weiyuan, China Due to Hydraulic Fracturing. *Journal of Geophysical Research: Solid Earth* **127** (5), e2021JB022963 (2022), doi:10.1029/2021JB022963.

36. W. Zhu, K. L. Allison, E. M. Dunham, Y. Yang, Fault valving and pore pressure evolution in simulations of earthquake sequences and aseismic slip. *Nature Communications* **11** (1), 4833 (2020), doi:10.1038/s41467-020-18598-z.

37. D. R. Faulkner, *et al.*, A Review of Recent Developments Concerning the Structure, Mechanics and Fluid Flow Properties of Fault Zones. *Journal of Structural Geology* **32** (11), 1557–1575 (2010), doi:10.1016/j.jsg.2010.06.009.

38. W. Zhao, *et al.*, Coupled Evolution of Seismicity and Permeability in Fault Zones. *Communications Earth & Environment* **6** (1), 918 (2025), doi:10.1038/s43247-025-02838-5.

39. Y. Ye, *et al.*, Injected Fluids Both Trigger and Facilitate a Cascade of Larger Earthquake Ruptures. *Earth and Planetary Science Letters* **687**, 120092 (2026), doi:10.1016/j.epsl.2026.120092.

40. G. M. Atkinson, D. W. Eaton, N. Igonin, Developments in Understanding Seismicity Triggered by Hydraulic Fracturing. *Nature Reviews Earth & Environment* **1** (5), 264–277 (2020), doi:10.1038/s43017-020-0049-7.

41. L. De Barros, D. Marsan, Theoretical Maximum and Cumulative Seismic Moment Relationships Confirm that Injection Volume Controls the Occurrence Rate, But Not the Magnitude, of Induced Earthquakes. *Geophysical Research Letters* **53** (5), e2025GL117164 (2026), doi:10.1029/2025GL117164.

42. L. Buijze, *et al.*, Review of Induced Seismicity in Geothermal Systems Worldwide and Implications for Geothermal Systems in the Netherlands. *Netherlands Journal of Geosciences* **98**, e13 (2019), doi:10.1017/njg.2019.6.

43. N. J. van der Elst, M. T. Page, D. A. Weiser, T. H. Goebel, S. M. Hosseini, Induced earthquake magnitudes are as large as (statistically) expected. *Journal of Geophysical Research: Solid Earth* **121** (6), 4575–4590 (2016), doi:10.1002/2016JB012818.

44. G. R. Foulger, M. P. Wilson, J. G. Gluyas, B. R. Julian, R. J. Davies, Global Review of Human-Induced Earthquakes. *Earth-Science Reviews* **178**, 438–514 (2018), doi:10.1016/j.earscirev.2017.07.008.

45. Y. Qin, *et al.*, Deciphering the Stress State of Seismogenic Faults in Oklahoma and Southern Kansas Based on an Improved Stress Map. *Journal of Geophysical Research: Solid Earth* **124** (12), 12920–12934 (2019), doi:10.1029/2019JB018377.

46. J. H. Norbeck, R. N. Horne, Maximum magnitude of injection-induced earthquakes: A criterion to assess the influence of pressure migration along faults. *Tectonophysics* **733**, 108–118 (2018), doi:10.1016/j.tecto.2018.01.028.

47. S. Ozawa, R. Ando, E. M. Dunham, Quantifying the probability of rupture arrest at restraining and releasing bends using earthquake sequence simulations. *Earth and Planetary Science Letters* **617**, 118276 (2023), doi:10.1016/j.epsl.2023.118276.

48. L. Li, K. Im, J.-P. Avouac, Large-Magnitude Events Unlikely in Induced Earthquake Sequences. *Nature Communications* **17** (1), 4192 (2026), doi:10.1038/s41467-026-72219-9.

49. S. Ozawa, Partial Ruptures, Cascading Multi-Fault Ruptures, and Aftershocks in 2D Random Fault Network. *Geophysical Research Letters* **53** (8), e2025GL120375 (2026), doi:10.1029/2025GL120375.

50. Y. Cheng, *et al.*, Seismicity Induced by Geological CO_2 Storage: A Review. *Earth-Science Reviews* **239**, 104369 (2023), doi:10.1016/j.earscirev.2023.104369.

51. Oklahoma Geological Survey, Earthquake origin for the 3 February 2024 Prague, Oklahoma, earthquake (event ok2024cish), Oklahoma Geological Survey origin product archived by the U.S. Geological Survey (2024), `https://earthquake.usgs.gov/product/origin/ogs2024cish/ok/1707409689255/quakeml.xml`, origin at 35.53433333 degrees N, 96.76383333 degrees W; accessed 8 September 2026.

52. U.S. Geological Survey, Earthquake origin for the 3 February 2024 Prague, Oklahoma, earthquake (event us7000lwmc), U.S. Geological Survey reviewed origin product (2024), `https://earthquake.usgs.gov/product/origin/us7000lwmc/`

`us/1713036954040/quakeml.xml`, origin at 35.5446 degrees N, 96.7390 degrees W; product version 1713036954040; accessed 12 September 2026.

53. A. Mignan, M. Broccardo, S. Wiemer, D. Giardini, Induced Seismicity Closed-Form Traffic Light System for Actuarial Decision-Making During Deep Fluid Injections. *Scientific Reports* **7** (1), 13607 (2017), doi:10.1038/s41598-017-13585-9.

54. J. Zhang, W. Kuang, X. Zhang, C. Mo, D. Zhang, Global Review of Induced Earthquakes in Oil and Gas Production Fields. *Reviews of Geophysics and Planetary Physics* **52** (3), 239–265 (2021), doi:10.19975/j.dqyxx.2020-027.

55. X. Bao, D. W. Eaton, Fault activation by hydraulic fracturing in western Canada. *Science* **354** (6318), 1406–1409 (2016), doi:10.1126/science.aag2583.

56. F. Catalli, A. P. Rinaldi, V. Gischig, M. Nespoli, S. Wiemer, The Importance of Earthquake Interactions for Injection-Induced Seismicity: Retrospective Modeling of the Basel Enhanced Geothermal System. *Geophysical Research Letters* **43** (10), 4992–4999 (2016), doi:10.1002/2016GL068932.

57. P. Romanet, J.-P. Ampuero, F. Cappa, M. M. Scuderi, S. Chaillat, Combined Boundary Element and Finite Volume Methods for Modelling Fluid-Induced Seismicity in Fault Networks Within Low-Permeability Rocks. *Geophysical Journal International* **243** (3), ggaf377 (2025), doi:10.1093/gji/ggaf377.

58. M. Cocco, J. R. Rice, Correction to "Pore Pressure and Poroelasticity Effects in Coulomb Stress Analysis of Earthquake Interactions". *Journal of Geophysical Research: Solid Earth* **108** (B2), 2069 (2003), doi:10.1029/2002JB002319.

59. S. Barbot, Y. Fialko, A Unified Continuum Representation of Post-Seismic Relaxation Mechanisms: Semi-Analytic Models of Afterslip, Poroelastic Rebound and Viscoelastic Flow. *Geophysical Journal International* **182** (3), 1124–1140 (2010), doi: 10.1111/j.1365-246X.2010.04678.x.

60. A. H.-D. Cheng, *Poroelasticity*, vol. 27 of *Theory and Applications of Transport in Porous Media* (Springer, Cham, Switzerland) (2016), doi:10.1007/978-3-319-25202-5.

Acknowledgments

Funding: The authors received no specific funding for this work.

Author contributions: Z.L.: Conceptualization, Methodology, Software, Validation, Formal analysis, Investigation, Visualization, Writing – original draft, Writing – review & editing. S.B.: Conceptualization, Methodology, Supervision, Writing – review & editing.

Competing interests: The authors declare that they have no competing interests.

Data and materials availability: Code, numerical data, and supplementary movies supporting the results of this study have been deposited in Zenodo and will be made publicly available upon publication. Reviewer access will be provided with the submission.

Supplementary Materials

Materials and Methods

Figs. S1 to S6

Tables S1 to S6

Captions for Movies S1 to S2

References *(57–60)*

Movies S1 to S2

Supplementary Materials for

Undrained fault-zone poroelastic feedback enables the 2011 Prague earthquake cascade

Zhengze Li*, Sylvain Barbot

*Corresponding author. Email: zhengzel@usc.edu

This PDF file includes:

Materials and Methods

Figures S1 to S6

Tables S1 to S6

Captions for Movies S1 to S2

References *(57–60)*

Other Supplementary Materials for this manuscript:

Movies S1 to S2

References are numbered consistently with the main manuscript and are listed there.

Materials and Methods

Prague sequence constraints and fault-network representation

We represented the Prague fault system in a two-dimensional east–north plane using two network configurations. The simulations in Figures 2–4 used a three-fault model containing only the principal rupture segments of the Prague sequence. Faults 1–3 were inferred from relocated seismicity, focal mechanisms, and published rupture interpretations (*17, 20–22*). The simulations in Figure 5 used an extended representation containing 27 fault segments. The extended fault-network geometry was constructed by digitizing the fault-network map presented by Cochran et al. (*22*), which was based on the mapped Wilzetta fault geometry of Way (*19*). Faults 1–3 represent the primary Prague sequence, whereas Faults 4–27 are designated receiver faults for the post-sequence analysis. The two configurations were discretized into 165 and 426 elements, respectively. Within each model configuration, segment endpoints and discretization were identical in the hydraulic, elastic-kernel, long-term loading, and injection-restart calculations; the code checks element-center agreement before coupling the model components.

Table S1 reports the exact fault geometries used in the two model configurations. Coordinates are given in the local Cartesian system used by the simulations, with x positive eastward, y positive northward, and the origin located at 96.82°W, 35.50°N. The listed start and end points preserve the endpoint ordering used in the numerical model. Each straight segment was subdivided uniformly into N_e fault elements. Faults 1 and 2 have configuration-specific endpoints in the three-fault and extended-network models, whereas the endpoints of Fault 3 are unchanged.

Both network configurations used regional compression axes assigned from the local stress field, with SHmax oriented 73° clockwise from north and compression-positive principal stresses of 90 and 46 MPa. For each element, the normal vector was selected consistently and the positive slip direction was chosen as the direction favored by the resolved regional shear stress. This convention prevents endpoint ordering from changing the sign of inter-fault stress transfer.

Adaptive finite-volume simulation of pore-pressure diffusion

Pressure evolution was calculated on an adaptive quadtree finite-volume grid. The initial square domain is 25.6 km wide, and refinement levels 5–9 concentrate the smallest cells around the mapped fault damage zones. Each fault element was mapped to its nearest finite-volume cell so that the calculated pressure history could be sampled directly along the mechanical model geometry.

We derived the pressure equation from quasistatic poroelasticity in a homogeneous, isotropic full space under plane strain. The poroelastic material parameters are spatially uniform, while permeability varies between the host rock and fault damage zones. Mechanical equilibrium gives

$$\mu\nabla^2\mathbf{u} + (\lambda+\mu)\nabla\epsilon_v - \alpha_h\nabla P = 0, \tag{S1}$$

where $\mathbf{u}$ is displacement, $\epsilon_v = \nabla\cdot\mathbf{u}$ is volumetric strain, λ and μ are the drained Lamé moduli, and α_h is the hydraulic-model Biot coefficient. The pressure gradient acts as an equivalent body force $-\alpha_h\nabla P$. Taking the divergence gives

$$\nabla^2[(\lambda+2\mu)\epsilon_v - \alpha_h P] = 0. \tag{S2}$$

For localized injection-induced perturbations that vanish at infinity,

$$\epsilon_v = \frac{\alpha_h P}{\lambda+2\mu}. \tag{S3}$$

The increment of fluid content per unit reference bulk volume is therefore

$$\zeta = \alpha_h\epsilon_v + \frac{P}{M_B} = S_{\text{eff}}P, \qquad S_{\text{eff}} = \frac{1}{M_B} + \frac{\alpha_h^2}{\lambda+2\mu}, \tag{S4}$$

where M_B is the Biot modulus and S_{eff} is the effective storage coefficient. Combining fluid mass conservation with Darcy's law gives

$$S_{\text{eff}}\frac{\partial P}{\partial t} = \nabla\cdot\left(\frac{k}{\mu_f}\nabla P\right) + q_v, \tag{S5}$$

where k is permeability, μ_f is fluid viscosity, and q_v is the volumetric fluid-source rate per unit bulk volume, positive for injection. For spatially uniform S_{eff} and μ_f, the resulting pressure equation is

$$\frac{\partial P}{\partial t} = \nabla \cdot (D \nabla P) + s_P(\mathbf{x}, t), \tag{S6}$$

where P is the pressure perturbation, D is hydraulic diffusivity, and $s_P = q_v/S_{\text{eff}}$ is the pressure-rate source term. The composite hydraulic coefficient is

$$\mathcal{C}_h = \mu_f S_{\text{eff}} = \frac{\mu_f}{M_B} \frac{\lambda + 2\mu + \alpha_h^2 M_B}{\lambda + 2\mu}, \qquad D = \frac{k}{\mathcal{C}_h}, \tag{S7}$$

The units of S_{eff} and $\mathcal{C}_h$ are Pa^{-1} and s, respectively. The hydraulic coefficients follow the standard Biot relations given below, with α_h and B_h denoting their hydraulic-model values. For a two-dimensional source rate $q_{\text{2D}}(t)$ applied to finite-volume cell i with area A_i, the source term is

$$s_{P,i}(t) = \frac{\mu_f q_{\text{2D}}(t)}{\mathcal{C}_h A_i}. \tag{S8}$$

The transmissibility matrix was assembled from neighboring quadtree cells, and the diffusion operator was integrated in time using an implicit Crank–Nicolson scheme. For a fixed grid, diffusivity field, and time step, the sparse matrix on the left-hand side of the Crank–Nicolson system remained constant. We therefore factorized this matrix once using a sparse LU decomposition and reused the factorization at every time step, updating only the right-hand side. The 100-year pressure calculation used for the post-sequence fault-network experiments in Figure 5 employed 2000 uniform time steps, corresponding to 20 steps per year. The non-intermittent operational experiments in Figs. 4A, 4B, and 4D likewise used approximately 20 uniform steps per year, with the total number of steps scaled to the simulated duration. The intermittent-injection experiments in Figure 4C used 6000 uniform steps over 100 years, corresponding to 60 steps per year ($\Delta t \approx 6.08$ days), except for the $T_r = 3$ d cases, which used 20,000 steps over 100 years, corresponding to 200 steps per year ($\Delta t \approx 1.83$ days). A 30-day linear startup ramp was applied in the continuous-source calculations, whereas the intermittent experiments used the prescribed square-wave schedules without a startup ramp.

The adaptive finite-volume pressure solver was evaluated against the native diffusion implementation in DemystiFicatioN_DFN (*57*) using the matched configuration described in the Numerical benchmarks section and Fig. S1.

The reference material has Lamé parameters $\lambda = \mu = 30$ GPa, grain bulk modulus 100 GPa, fluid bulk modulus 2.25 GPa, porosity 0.01, and fluid viscosity 0.4 mPa s. With a reference host-rock permeability of approximately 8.4×10^{-18} m^2, these values give a background diffusivity of approximately 1.7×10^{-3} m^2 s^{-1}. Fault damage zones were assigned a diffusivity 1000 times the background value in the reference calculation. The injection-source location and reference volumetric well rate were based on the well records reported by Keranen et al. (*17*). We converted the three-dimensional volumetric well rate to an equivalent two-dimensional source rate using

$$q_{2D}(t) = \frac{Q_{3D}(t)}{h_{\mathrm{eff}}}, \qquad h_{\mathrm{eff}} \approx 1.78 \text{ km}, \tag{S9}$$

where h_{eff} is the effective out-of-plane flow thickness. This conversion yields the reference source rate $q_{\mathrm{ref}} \approx 1.7 \times 10^{-7}$ m^2 s^{-1}. Injection was maintained throughout the simulations in Figures 2 and 3. For the operational experiments in Figure 4, the steady-rate, intermittent, and injection–extraction schedules were maintained until first nucleation, whereas the finite-duration source-distance suite prescribed 18 years of injection followed by shut-in and continued evolution to first nucleation. For the post-sequence fault-network simulations in Figure 5, injection was terminated at model year 19, after the reproduced Prague sequence, to evaluate the subsequent response of the surrounding fault network. The post-sequence interval therefore includes continued injection from sequence end to model year 19, followed by post-shut-in evolution. Pressure histories and selected full-field snapshots were stored for the fault-dynamics and visualization calculations.

Elastic fault interactions

Shear- and normal-stress interactions were calculated with Galerkin boundary-element kernels using triangular slip basis functions. The medium was homogeneous and elastic with shear modulus $\mu = 30$ GPa and Poisson ratio $\nu = 0.25$. We derived analytical expressions for the two-dimensional Galerkin interaction kernels between distinct elements and benchmarked them against independent Fourier-domain calculations and high-order numerical quadrature; the full derivations and validation tests are provided in the Supplementary Materials (Figs. S2 and S3). Self-interactions were evaluated by high-order numerical quadrature, and the kernel sign conventions were further verified by requiring negative self shear stiffness.

For slip vector δ, the elastic shear- and total normal-stress perturbations are

$$\Delta\tau = K_s\delta, \qquad \Delta\sigma_n = K_n\delta, \tag{S10}$$

where normal stress is positive in compression. Both matrices include interactions within and between faults. Radiation damping was included through $\eta = \mu/(2\mathrm{Vs})$, with shear-wave speed $\mathrm{Vs} = 3$ km s^{-1}.

Rate-and-state friction and effective fault-zone poroelastic feedback

All fault elements obeyed the following friction law (*25*):

$$f = f_0 \exp\left[\frac{a}{f_0}\ln\left(\frac{V}{V_0}\right) + \frac{b}{f_0}\Phi\right], \tag{S11}$$

with state evolution

$$\dot{\Phi} = \frac{V_0 e^{-\Phi} - V}{L}. \tag{S12}$$

The reference values were $f_0 = 0.6$, $V_0 = 10^{-6}$ m s^{-1}, and $L = 0.002$ m. Most fault interiors were velocity weakening with $a = 0.005$ and $b = 0.007$, whereas selected fault tips approached velocity-strengthening values of $a = 0.010$ and $b = 0.005$.

In the three-fault model, the characteristic tip-transition length was $L_{\mathrm{tip}} = \min(0.1L_f,$ 1 km), where L_f is the corresponding fault-segment length; the transition was applied at the designated outer tips of the modeled network. In the 27-fault model, a fixed $L_{\mathrm{tip}} =$ 500 m was applied at terminal network tips. An endpoint lying within 150 m of another fault segment was classified as attached and was therefore not treated as terminal. In both configurations, the friction parameters were interpolated with a hyperbolic-tangent function having a smoothing width of $L_{\mathrm{tip}}/3$. Quasi-dynamic force balance was

$$\tau = \sigma_n' f + \eta V. \tag{S13}$$

Effective normal stress combined background stress, injection pressure, elastic normal-stress transfer, and a reduced-order representation of the rapid local fault-zone pore-pressure response. For a homogeneous isotropic poroelastic material under undrained conditions, the pore-pressure change is related to the mean total-stress change by

$$\Delta P = B\Delta\sigma_m, \qquad \Delta\sigma_m = \frac{\Delta\sigma_{kk}}{3}, \tag{S14}$$

where compression is positive and B is the intrinsic Skempton coefficient. A narrow fault zone with elastic properties that differ from those of the surrounding rock has a more general response. Following Cocco and Rice (*27*), with the published corrections (*58*), its local undrained pore-pressure change can be written

$$\Delta P_f = B_f \frac{K_{u,f}}{H_{u,f}} \left[\frac{G_f}{G_h} \frac{H_{u,h}}{K_{u,h}} \Delta\sigma_m + \left(1 - \frac{G_f}{G_h}\right) \Delta\sigma_n \right], \tag{S15}$$

where the subscripts f and h denote fault-zone and host-rock properties, respectively, and $H_u = K_u + 4G/3$ is the undrained constrained modulus. This expression shows that mean and fault-normal stress changes generally both contribute. The slip-mediated normal-stress change was evaluated from the elastic interaction calculation as

$$\Delta\sigma_{n,\text{slip}} = K_n \delta. \tag{S16}$$

When the fault zone is sufficiently compliant relative to the surrounding rock ($G_f \ll G_h$), the response approaches

$$\Delta P_{\text{slip}} \approx \widehat{B} \Delta\sigma_{n,\text{slip}}, \qquad \widehat{B} = B_f \frac{K_{u,f}}{H_{u,f}}. \tag{S17}$$

Thus, $\widehat{B}$ is the effective pore-pressure response coefficient in the fault-normal-stress-dominated limit, which arises for an isotropic fault zone when $G_f/G_h \ll 1$ and may also arise from strong fault-zone anisotropy. In the latter case, $\widehat{B}$ is determined by the fault-normal component of the Skempton tensor (*27*).

We used the fault-normal-stress-dominated limit as a subgrid closure for unresolved fault damage-zone deformation and defined

$$\beta_{\text{eff}} = \alpha \widehat{B}, \tag{S18}$$

where β_{eff} is the effective fraction of slip-mediated normal-stress transfer buffered by the local pore-pressure response. At the level of the reduced normal-stress scaling, this formulation is algebraically equivalent to the conventional effective-friction relation $\mu' = \mu(1-\beta)$ used by Sumy et al. (*18*) in their static Coulomb analysis. In the present model, β_{eff} was applied continuously within the evolving rate-and-state fault-network calculation. The effective-pressure coefficient in the fault-dynamics calculation was fixed at $\alpha = 1$, distinct from the hydraulic-model Biot coefficient $\alpha_h = 0.50$, so the parameter varied numerically in the code is $\beta_{\text{eff}} = \widehat{B}$. We set $\beta_{\text{eff}} = 1$ in the Figure 2 reference simulation and in all post-sequence fault-network simulations shown in Figure 5. The corresponding slip-mediated effective-normal-stress change is

$$\Delta\sigma'_{n,\text{slip}} = \Delta\sigma_{n,\text{slip}} - \alpha\Delta P_{\text{slip}} = (1-\beta_{\text{eff}})\Delta\sigma_{n,\text{slip}}. \tag{S19}$$

Total effective normal stress was therefore evaluated as

$$\sigma'_n = \sigma_{n,0} - \alpha\left(P_0 + P_{\text{inj}}\right) + (1-\beta_{\text{eff}})K_n\delta. \tag{S20}$$

Here $P_0 = 30$ MPa and P_{inj} is interpolated from the finite-volume calculation. Slip-induced normal-stress changes generated an undrained pore-pressure response that fed back on effective normal stress and fault strength. The slip-induced term affected fault strength instantaneously but was not propagated through the finite-volume pressure field; the formulation therefore represents the local undrained limit rather than the subsequent redistribution or relaxation of slip-induced pressure. Because $K_n\delta$ was already evaluated in the elastic interaction calculation, including this feedback required only multiplying the slip-mediated normal-stress contribution by $1-\beta_{\text{eff}}$. It introduced no additional diffusion solve or state variables and therefore retained a computational cost nearly identical to that of the same model with slip-induced pore-pressure feedback disabled.

We used standard isotropic Biot relations to evaluate plausible intrinsic and effective end-member coupling values (*59, 60*). The drained and undrained bulk moduli and poroelastic coefficients were related by

$$K_d = \lambda + \frac{2}{3}\mu, \qquad \alpha = 1 - \frac{K_d}{K_s}, \tag{S21}$$

$$M_B^{-1} = \frac{\alpha - \phi}{K_s} + \frac{\phi}{K_f}, \qquad K_u = K_d + \alpha^2 M_B, \tag{S22}$$

and

$$B = \frac{\alpha M_B}{K_u}, \qquad \alpha B = \frac{\alpha^2 M_B}{K_u} = 1 - \frac{K_d}{K_u}, \tag{S23}$$

where M_B is the Biot modulus, distinguished here from the constrained modulus H_u. In these material relations, α denotes the intrinsic Biot coefficient rather than the prescribed effective-pressure coefficient in the fault-dynamics calculation. Using $K_s = 100$ GPa, $K_f = 2.25$ GPa, and $\phi = 0.01$, together with $\lambda = \mu = 30$ GPa for the reference rock, gives $\alpha = 0.50$, $B = 0.70$, and the intrinsic product $\alpha B = 0.35$. Reducing the drained Lamé parameters to $\lambda = \mu = 3$ GPa as an illustrative compliant damage-zone end member gives $\alpha = 0.95$, $B = 0.98$, and $\alpha B = 0.93$. Applying the compliant isotropic fault-zone mapping $\beta_{\text{eff}} = \alpha B K_u / H_u$ to this end member gives $\beta_{\text{eff}} \approx 0.88$. These calculations show that the upper portion of the explored effective-coupling range is physically plausible, but they are illustrative material end members rather than direct estimates of Prague fault-zone properties. The reference elastic kernels did not explicitly resolve a compliant or anisotropic fault-zone layer; its rapid local response was represented through the effective parameter β_{eff}.

The coupled ordinary differential equations for slip, state, and logarithmic velocity were integrated with MATLAB's `ode15s` solver. Solving for log velocity improves numerical stability across the many orders of magnitude separating interseismic creep and dynamic rupture.

We benchmarked the combined Galerkin boundary-element and rate-and-state implementation against DEMYSTIFICATION_DFN (*57*) using matched single-fault and parallel-fault configurations, including tests with and without fluid injection. The two implementations produced consistent recurrent stick-slip behavior and closely comparable event counts, nucleation and recurrence times, cumulative slip, and injection-driven fault response. The benchmark setups and quantitative comparisons are documented in the Supplementary Materials.

Long-term loading and prestress initialization

Initial fault stress was generated through long-term model evolution rather than assigned independently to every element. We adopted a horizontal regional stress tensor with an SHmax azimuth of 73°, which lies within the 95% bootstrap confidence region of the regional stress inversion by Sumy et al. (*18*), and stress magnitudes SHmax = 90 MPa and Shmin = 46 MPa. Because the absolute tectonic stressing rate is not independently constrained, the stress-rate tensor was used first to define the relative spatial pattern of loading. We assigned it the same principal directions and principal-stress ratio as the background stress and projected it onto the local orientation of each fault. The magnitude of the resulting resolved shear-stressing rate was converted into an element-wise long-term loading velocity, denoted V_L. Its absolute scale was then set by normalizing the distribution to an assumed mean velocity of 10^{-11} m s^{-1} and bounding individual values between 10^{-13} and 10^{-10} m s^{-1}. The elapsed model years reported below are therefore conditional on this prescribed loading scale and are used only to generate prestress templates; they are not estimates of the actual recurrence intervals or elapsed interseismic ages of the Prague faults.

Before long-term evolution, the prescribed regional stress tensor and the common background pore pressure $P_0 = 30$ MPa produced the fault-resolved initial conditions summarized in Table S3D. Because the three modeled faults are straight, these quantities were uniform along each fault. The common pore pressure did not produce identical effective normal stresses because the resolved shear and total normal tractions depended on fault orientation. The state variable was initialized as

$$\Phi_{0,i} = \ln\left(\frac{V_0}{V_{L,i}}\right), \tag{S24}$$

and the initial slip velocity was obtained from quasi-dynamic force balance. During the long-term calculation, shear stress evolved through back-slip loading,

$$\tau(t) = \tau_0 + K_s \left[\delta(t) - V_L t\right]. \tag{S25}$$

Because the self shear stiffness is negative, an element slipping more slowly than its loading velocity accumulates positive shear stress. Continued loading of the velocity-weakening fault interiors, together with elastic interactions within and among the three faults, therefore generated repeated instabilities without requiring fault-specific pore pressures.

For the three-fault simulations in Figures 2–4, we first evolved the system for 5000 years without injection under this background stress and loading-rate distribution. The resulting trajectory sampled repeated variations in shear stress, effective normal stress, frictional state, and slip rate. We selected the state at year 4300 as the prestress template for the injection calculation. Shear stress, effective normal stress, and the rate-and-state variable were inherited from this snapshot; incremental slip was reset to zero to avoid counting the inherited elastic stress twice, and initial velocity was recomputed from force balance.

We then applied one spatially uniform shear-stress adjustment to each of Faults 1–3 while retaining the element-to-element stress variations inherited from the year-4300 state. For the Figure 2 reference simulation, the adjustments were −0.015, +0.003, and +0.204 MPa for Faults 1–3, respectively. Their absolute values correspond to 0.75%, 0.21%, and 11.2% of the respective minimum-to-maximum ranges of fault-mean shear stress sampled during the 5000-year calculation. After adjustment, the shear stress on every element of each fault remained within that element's own long-term sampled minimum-to-maximum range. The adjustments therefore shifted each fault as a whole without independently tuning individual elements or altering the inherited along-fault stress heterogeneity. Separately calibrated fault-wide adjustments used for the β_{eff} experiments are reported in Table S2A. The long-term loading velocity was used only to generate the prestress template and was set to $V_L = 0$ throughout all subsequent injection and post-injection calculations in Figures 2–4. The modeled sequence therefore evolved from the selected and fault-level-adjusted prestress under hydraulic forcing, rate-and-state friction, and internal elastic and poroelastic interactions, without additional far-field loading. The hydraulic-property experiments in Figure 3D and all operational experiments in Figure 4 retained the Figure 2 reference prestress adjustments without case-specific retuning.

The post-sequence fault-network experiments in Figure 5 used an analogous but separate initialization of the 27-fault system. We evolved that system for 3000 years without injection and extracted its state at year 2930. The inherited shear stress, effective normal stress, and state variable were used as the prestress template; incremental slip was reset, initial velocity was recomputed from force balance, and $V_L = 0$ was again imposed throughout the subsequent injection and calculation to model year 100. For Faults 4–27, we first shifted each fault by a single scalar so that its spatially averaged shear stress matched the 0–3000-year space-time mean of that fault. This retained the within-fault stress heterogeneity of the year-2930 state. We then applied the same uniform prestress offset, ranging from 0 to +0.5 MPa in the experiments shown in Figure 5, to every receiver fault. For each receiver-fault prestress case, small fault-wide shear-stress adjustments to Faults 1–3 were determined separately, within their long-term sampled stress ranges and without altering the inherited along-fault stress heterogeneity, so that the model reproduced the calibrated Prague sequence. The resulting adjustments and sequence metrics are reported in Table S2B. Faults 1–3 were not included in the common receiver-fault prestress offset.

For the Figure 5 calibration, the accepted intervals were 17.5–18.0 years for Fault 1 dynamic rupture, 0.8–1.2 days for Δt_{12}, and 1.8–2.5 days for Δt_{23}, together with the Fault 1–Fault 2–Fault 3 rupture order. All three primary faults were required to reach $V_{\max,f} \geq 10^{-2}\ \mathrm{m\,s^{-1}}$, and their modeled magnitudes were checked for consistency with the Prague sequence.

Numerical parameter values are rounded for presentation.

Values were calculated before long-term earthquake-cycle evolution and before any fault-wide prestress adjustment. The subscript 0 denotes the beginning of the long-term calculation, the subscript n denotes the fault-normal component, and the prime denotes effective rather than total normal stress. Here, τ_0 is the initial shear stress resolved in the modeled slip direction, $\sigma_{n,0}$ is the initial total normal stress, positive in compression, and $\sigma'_{n,0} = \sigma_{n,0} - \alpha P_0$ is the initial effective normal stress, with the common $P_0 = 30$ MPa and $\alpha = 1$. The symbol V_L denotes the imposed long-term loading velocity, where the subscript L denotes loading; it was derived from the regional stress-rate pattern resolved onto each fault. The transformed initial state variable is

$$\Phi_0 = \ln\left(\frac{\theta_0 V_0}{L}\right) = \ln\left(\frac{V_0}{V_L}\right), \tag{S26}$$

where θ_0 is the conventional initial state variable, V_0 is the reference slip velocity, and L is the state-evolution distance. The second equality follows from assigning the steady-state condition $\theta_0 = L/V_L$ at the beginning of the long-term calculation. Because each of the three modeled faults is straight, the listed quantities are uniform along each fault; the element index i, used elsewhere for element-wise quantities, is therefore omitted here. The dimensionless ratio $\tau_0/\sigma'_{n,0}$ describes the modeled initial stress state but is not treated as a fixed failure criterion under rate-and-state friction.

Parameter experiments and event metrics

The parameter experiments were designed to examine how hydraulic loading acts on an initially prestressed fault system, how rupture transfers between the primary faults, and how receiver faults respond after the primary sequence.

The effective-coupling experiments sampled $\beta_{\text{eff}} = 0$, 0.25, 0.50, 0.65, 0.75, 0.85, 0.90, and 1.0. At each β_{eff}, the three fault-wide prestress offsets were optimized to obtain the closest overall reproduction of the observed Prague sequence, and the best-matching simulation was retained for the comparisons in Figures 3A–C. The selection considered the Fault 1 nucleation time, both interevent intervals, and the Fault 3 response, evaluated from its approximate magnitude and maximum slip rate. The exact shear-stress adjustments and resulting sequence-response metrics are reported in Table S2A. In contrast, the hydraulic experiments held the mechanical, frictional, prestress, and injection parameters of the Figure 2 reference simulation fixed while independently varying the host-rock and damage-zone diffusivities. For each diffusivity pair, we recorded the time and location of first nucleation and whether each of Faults 1–3 subsequently reached the dynamic-rupture threshold. Operational experiments varied source–fault distance, steady injection rate, injection/shut-in cycles, and the ratio of extraction to injection. In the source-distance experiments (Figure 4A), one suite maintained continuous injection until first nucleation. A second suite imposed the reference injection rate for the full 18-year schedule at every source location, including cases that nucleated during injection; Figure 4A records only the first nucleation time, and cases without prior nucleation were continued after shut-in until it occurred. The 18-year duration corresponds to the approximate injection-to-Fault 1 nucleation time in the calibrated Prague reference simulation and was adopted as a common finite operational horizon across source locations. A no-injection control was evolved from the same initialized prestress state with $q_{2D} = 0$. Because $V_L = 0$ in all operational experiments, this control provides the reference for measuring how strongly injection advances nucleation. In the steady-rate, intermittent, and injection–extraction experiments (Figures 4B–D), the prescribed schedules were maintained until first nucleation. Steady-injection cases maintained a constant rate, injection–extraction cases maintained both source rates, and intermittent cases repeated the prescribed on/off cycle. In the intermittency tests, one suite held the peak rate fixed, whereas a second adjusted the peak rate to preserve the cycle-averaged rate. Exact parameter grids, source locations, and operational schedules are summarized in Table S4.

The 24 combinations listed above are the cells with simulation results in Figure 3D; the remaining six cells in the nominal five-by-six grid were not run. Across this experiment, the Figure 2 mechanical, frictional, prestress, and injection parameters were held fixed, with no case-specific prestress retuning.

All source-distance experiments used $q_{2D} = q_{ref}$. The no-injection control used $q_{2D} = 0$ and the same initialized fault state.

The intermittent experiments used square-wave injection without the 30-day startup ramp applied in the continuous-source calculations.

Auxiliary source-distance calculations

We performed two auxiliary calculations to quantify the source-distance effects discussed in the main text. First, because the continuous-injection distance experiments used the same prescribed source rate and 30-day ramp at every location, cumulative two-dimensional fluid input before nucleation was calculated as $I_{2D}(t_n) = \int_0^{t_n} q_{2D}(t)\, dt$. First nucleation occurred at 18.0 years for the calibrated source 0.143 km from the fault network and at 241.9 years for the farthest source at 9.15 km. The corresponding cumulative input ratio was approximately 13.4, or approximately 13 when rounded to the precision used in the main text.

Second, we isolated the hydraulic response to the finite-duration operation at the farthest source. The calculation used the three-fault geometry, $D_{\mathrm{bg}} = 1.74 \times 10^{-3}\ \mathrm{m^2\,s^{-1}}$, $D_{\mathrm{dz}} = 1.74\ \mathrm{m^2\,s^{-1}}$, $q_{\mathrm{2D}} = q_{\mathrm{ref}}$, the 30-day source ramp, and a uniform time step of 1/12 year. Injection was terminated at 18 years, after which pressure diffusion was continued to 1000 years. Fault 1 pressure was evaluated as the element-length-weighted mean

$$\overline{P}_1(t) = \frac{\sum_{i \in F_1} L_i P_i(t)}{\sum_{i \in F_1} L_i}. \tag{S27}$$

At the 9.15-km source distance, $\overline{P}_1$ reached a post-shut-in maximum of 0.01266 MPa at approximately 798 years and remained below 0.1 MPa throughout the 1000-year calculation. The value reported in the main text was therefore rounded to 0.013 MPa. This auxiliary calculation quantifies hydraulic attenuation with distance; the corresponding coupled nucleation times additionally reflect rate-and-state evolution and internal fault interactions.

We classified an element as activated or nucleating when $V_i \geq 10^{-4}\ \mathrm{m\,s^{-1}}$. For the hydraulic and operational experiments, we report the first time any fault element reaches this velocity as the time to rupture initiation in the main text and figures. For fault f, we defined

$$V_{\max,f} = \max_t \max_{i \in f} V_i(t), \tag{S28}$$

and classified the fault as dynamically rupturing when $V_{\max,f} \geq 10^{-2}\ \mathrm{m\,s^{-1}}$. Event onset was the first time any element on a fault crossed the corresponding threshold. Activated length was the summed length of threshold-crossing elements. For event e, the dynamically accumulated slip of element i was calculated as

$$D_{i,e}^{\mathrm{dyn}} = \sum_{n \in e} \left| \delta_i^{n+1} - \delta_i^n \right| \mathcal{I}\left[\max\left(V_i^n, V_i^{n+1} \right) \geq V_{\mathrm{dyn}} \right], \qquad V_{\mathrm{dyn}} = 10^{-2}\ \mathrm{m\,s^{-1}}, \tag{S29}$$

where $\mathcal{I}$ is the indicator function. The rupture lengths reported for the primary Prague sequence were calculated by summing the lengths of elements that reached $V \geq 10^{-2}\ \mathrm{m\,s^{-1}}$ during each primary event. For the selected primary event on each fault, scalar seismic moment and moment magnitude were calculated from all dynamically accumulated slip increments within the event window as

$$M_{0,e} = \mu W \sum_i L_i D_{i,e}^{\mathrm{dyn}}, \qquad M_{w,e} = \frac{2}{3}\left[\log_{10}\left(\frac{M_{0,e}}{\mathrm{N\,m}}\right) - 9.1\right], \tag{S30}$$

where L_i is element length and $W = 3.5$ km is the assumed out-of-plane seismogenic width. When multiple dynamic episodes occurred on one fault, the primary event was selected as the episode with the largest scalar moment evaluated over elements with $D_{i,e}^{\mathrm{dyn}} \geq 0.01$ m. The dependence of the reported magnitude on the assumed width follows

$$M_w(W) = M_w(W_0) + \frac{2}{3}\log_{10}\left(\frac{W}{W_0}\right), \qquad W_0 = 3.5 \text{ km}. \tag{S31}$$

The post-sequence fault-network experiments in Figure 5 were conditioned on preserving the calibrated Prague sequence. In every analyzed simulation, we verified the injection-to-Fault 1 nucleation time, both interevent delays, the three-fault rupture order, and the modeled magnitudes for an assumed seismogenic width of $W = 3.5$ km. Sequence end was defined as the first time after Fault 3 reached the dynamic-rupture threshold at which all Fault 3 elements had returned below $V = 10^{-2}$ $\mathrm{m\,s^{-1}}$. The stress changes shown in Figure 5A were evaluated at sequence end relative to the injection-onset state. Shear-stress changes were calculated from modeled slip accumulated through sequence end, whereas effective-normal-stress changes include the hydraulic and slip-mediated contributions represented in the coupled model. Receiver response was measured as the maximum velocity from sequence end to model year 100. The lower panels show the first five years of post-sequence response on Faults 5 and 6; open circles mark the first crossing of the dynamic-rupture threshold. These choices distinguish receiver-fault response to a common primary sequence from comparisons among differently initiated sequences.

Numerical benchmarks

Component-level validation tests are organized separately from the Prague experiment descriptions so that each numerical implementation can be evaluated using matched geometry, forcing, boundary conditions, and comparison metrics.

Hydraulic diffusion benchmark

We compared the adaptive-quadtree finite-volume pressure solver used in this study with the native one-dimensional finite-volume diffusion implementation in DemystiFicatioN_DFN (*57*). The matched problem consisted of a 6-km-long horizontal fault damage zone with a central injection source, an initially zero pressure perturbation, and closed or effectively no-flow ends (Fig. S1A). The adaptive-quadtree calculation represented a nominally 200-m-wide damage zone in a two-dimensional domain. Its discrete high-diffusivity area corresponded to an effective width $W_{\mathrm{eff}} = 205$ m, and pressure was sampled at 50 uniformly spaced fault elements. The background diffusivity was set to a negligible value to isolate fault-parallel diffusion. The DemystiFicatioN_DFN calculation represented the same 6-km fault using 50 uniform one-dimensional control volumes of length 120 m; the central source was divided equally between the two middle control volumes. Both calculations used a matched diffusivity of

$$D = 9.9956 \times 10^{-2}\ \mathrm{m}^2\,\mathrm{s}^{-1} \approx 0.100\ \mathrm{m}^2\,\mathrm{s}^{-1}. \tag{S32}$$

Because the two solvers express hydraulic forcing using different source and storage conventions, we matched the effective line-source strength entering their one-dimensional pressure balances. In the adaptive-quadtree formulation, integrating the two-dimensional cell source across the discrete damage-zone width gives

$$\mathcal{S}_{\mathrm{AQ}} = \frac{\mu_f q_{\mathrm{2D}}}{\mathcal{C}_h W_{\mathrm{eff}}}, \tag{S33}$$

where μ_f is fluid viscosity, q_{2D} is the two-dimensional injection rate, and $\mathcal{C}_h$ is the composite hydraulic coefficient defined above. In the DemystiFicatioN_DFN formulation, the corresponding strength is

$$\mathcal{S}_{\mathrm{DFN}} = \frac{Q_{\mathrm{DFN}}}{S_f}, \qquad S_f = \phi_{\mathrm{DFN}} \left(\beta_f + \beta_\phi\right), \tag{S34}$$

where Q_{DFN} is the one-dimensional injection-rate parameter, S_f is fault-zone storage, ϕ_{DFN} is porosity, and β_f and β_ϕ are the fluid and pore-volume compressibilities. We prescribed $q_{\mathrm{2D}} = q_{\mathrm{ref}}$ in the adaptive-quadtree model and selected $Q_{\mathrm{DFN}} = 6.7721 \times 10^{-8}\ \mathrm{m}\,\mathrm{s}^{-1}$ so that

$$\mathcal{S}_{\mathrm{AQ}} = \mathcal{S}_{\mathrm{DFN}} = 67.7207\ \mathrm{Pa\,m\,s^{-1}}. \tag{S35}$$

The matched source was switched on at the start of both calculations and maintained at a constant value for 30 years without a startup ramp (Fig. S1B). Both solvers stored pressure at intervals of 0.025 year and used 10 internal substeps per output interval, giving an internal time step of 0.0025 year (approximately 0.913 day). The adaptive-quadtree solver used Crank–Nicolson time integration, whereas DemystiFicatioN_DFN used its native fully implicit finite-volume update. Table S5 summarizes the matched physical and numerical parameters.

We compared the fault-sampled pressure perturbations at every stored time. Taking the DemystiFicatioN_DFN solution as the reference, the time-dependent relative L_2 and L_∞ differences were defined as

$$\epsilon_2(t_n) = \frac{\left[\sum_{j=1}^{N}\left(P_{j,n}^{\mathrm{AQ}} - P_{j,n}^{\mathrm{DFN}}\right)^2\right]^{1/2}}{\left[\sum_{j=1}^{N}\left(P_{j,n}^{\mathrm{DFN}}\right)^2\right]^{1/2}}, \tag{S36}$$

$$\epsilon_\infty(t_n) = \frac{\max_j \left|P_{j,n}^{\mathrm{AQ}} - P_{j,n}^{\mathrm{DFN}}\right|}{\max_j \left|P_{j,n}^{\mathrm{DFN}}\right|}, \tag{S37}$$

where $N = 50$, j indexes fault samples, and n indexes stored times. The relative L_2 difference measures the root-sum-square discrepancy across the entire pressure profile, whereas the relative L_∞ difference measures the largest pointwise discrepancy relative to the maximum reference pressure at that time. We also calculated a global relative L_2 difference over all stored pressure fields,

$$\epsilon_{2,\mathrm{global}} = \frac{\left[\sum_n \sum_{j=1}^{N}\left(P_{j,n}^{\mathrm{AQ}} - P_{j,n}^{\mathrm{DFN}}\right)^2\right]^{1/2}}{\left[\sum_n \sum_{j=1}^{N}\left(P_{j,n}^{\mathrm{DFN}}\right)^2\right]^{1/2}}. \tag{S38}$$

The two calculations produced nearly coincident pressure profiles at 0.5, 1, 5, 10, and 30 years (Fig. S1C). The global relative L_2 difference was 0.00193. For the time-dependent comparisons shown from 0.5 years onward in Fig. S1D, the maximum relative differences were 0.0335 in L_2 and 0.0499 in L_∞; by 30 years, they had decreased to 0.00113 and 0.00255, respectively.

These comparisons verify that the adaptive-quadtree solver reproduces the fault-parallel pressure evolution of the independent DEMYSTIFICATION_DFN implementation under matched hydraulic conditions.

Closed-form tapered-source stress benchmark

The elastic interaction calculation begins by integrating the plane-strain stress Green's function over a triangular slip basis associated with each source element. We verified the resulting closed-form source kernel against an independent Fourier-domain calculation (Fig. S2). The support of the triangular basis occupied $-a \leq x \leq a$ in a source-local coordinate system, with prescribed slip

$$\delta(x) = \begin{cases} A\left(1 - |x|/a\right), & |x| \leq a, \\ 0, & |x| > a. \end{cases} \tag{S39}$$

For shear modulus μ and Poisson's ratio ν, define

$$C = \frac{\mu A}{2\pi(1-\nu)a}, \tag{S40}$$

$$R_+ = (x+a)^2 + y^2, \qquad R_0 = x^2 + y^2, \qquad R_- = (x-a)^2 + y^2, \tag{S41}$$

and

$$H = \frac{x+a}{R_+} - \frac{2x}{R_0} + \frac{x-a}{R_-}, \tag{S42}$$

$$L = \frac{1}{2}\left[\ln\left(\frac{R_+}{R_0}\right) - \ln\left(\frac{R_0}{R_-}\right)\right], \tag{S43}$$

$$G = \frac{1}{R_+} - \frac{2}{R_0} + \frac{1}{R_-}, \tag{S44}$$

$$\Theta = \tan^{-1}\left(\frac{x+a}{y}\right) - 2\tan^{-1}\left(\frac{x}{y}\right) + \tan^{-1}\left(\frac{x-a}{y}\right). \tag{S45}$$

The closed-form stresses implemented in the model are

$$\sigma_{yy}^{\mathrm{CF}} = CyH, \tag{S46}$$

$$\sigma_{xy}^{\mathrm{CF}} = -C\left(L + y^2 G\right), \tag{S47}$$

$$\sigma_{xx}^{\mathrm{CF}} = C\,(2\Theta - yH) = 2C\Theta - \sigma_{yy}^{\mathrm{CF}}. \tag{S48}$$

These expressions are identical to writing $C = \mu\alpha A/(\pi a)$ with the plane-strain coefficient $\alpha = [2(1-\nu)]^{-1}$. They were evaluated using the same branch convention as the production kernel.

The independent numerical reference was obtained by transforming the triangular slip distribution to the Fourier domain. With wavenumber k, $q = |k||y|$, and Fourier-transformed slip $\widehat{\delta}(k)$, the transfer relations were

$$\widehat{\sigma}_{xy} = -\mu\alpha|k|(1-q)e^{-q}\widehat{\delta}(k), \tag{S49}$$

$$\widehat{\sigma}_{yy} = i\mu\alpha kq\,e^{-q}\,\mathrm{sgn}(y)\widehat{\delta}(k), \tag{S50}$$

$$\widehat{\sigma}_{xx} = i\mu\alpha k(2-q)e^{-q}\,\mathrm{sgn}(y)\widehat{\delta}(k). \tag{S51}$$

We used $a = 100$ m, $A = 1$ m, $\mu = 30$ GPa, and $\nu = 0.25$. The spectral calculation used 2^{16} points in a periodic domain of length $200a$, while the comparison window was restricted to $-3 \leq x/a \leq 3$ and $-2 \leq y/a \leq 2$. The field-point grid was staggered about $y = 0$, so the singular source line itself was not sampled, but the solution was approached from both sides.

For each stress component, the plotted closed-form field and normalized absolute difference were defined relative to the maximum absolute value of the corresponding Fourier-domain solution,

$$\widetilde{\sigma}_{ij}^{\mathrm{CF}}(x,y) = \frac{\sigma_{ij}^{\mathrm{CF}}(x,y)}{\max_{x,y}|\sigma_{ij}^{\mathrm{F}}(x,y)|}, \tag{S52}$$

$$\epsilon_{ij}(x,y) = \frac{|\sigma_{ij}^{\mathrm{CF}}(x,y) - \sigma_{ij}^{\mathrm{F}}(x,y)|}{\max_{x,y}|\sigma_{ij}^{\mathrm{F}}(x,y)|}. \tag{S53}$$

The component-wise global relative L_2 difference was

$$\epsilon_{2,ij} = \frac{\|\sigma_{ij}^{\mathrm{CF}} - \sigma_{ij}^{\mathrm{F}}\|_2}{\|\sigma_{ij}^{\mathrm{F}}\|_2}. \tag{S54}$$

The global relative L_2 differences for σ_{xx}, σ_{xy}, and σ_{yy} were 4.59×10^{-5}, 3.74×10^{-4}, and 1.32×10^{-4}, respectively. The corresponding 99th-percentile normalized absolute differences were 3.43×10^{-6}, 1.22×10^{-5}, and 1.83×10^{-5}. The largest localized differences were 7.59×10^{-4},

3.24×10^{-3}, and 5.34×10^{-3}, respectively, and were confined to the immediate vicinity of the source plane and triangular-basis nodes (Fig. S2D–F).

Closed-form Galerkin receiver-integration benchmark

The second analytical integration projects the tapered-source stress onto a triangular basis on a receiver element. This step converts the pointwise source stress above into the source-to-receiver Galerkin interaction used in the fault-system calculations. We verified the analytical integration against direct high-order Gauss–Legendre quadrature over a systematic set of source–receiver geometries (Fig. S3).

Let the source have half-length a_s and center at the origin of a source-local coordinate system. The triangular source basis can be represented by three source nodes and weights,

$$x_j = \{a_s, 0, -a_s\}, \qquad \omega_j = \frac{1}{a_s}\{1, -2, 1\}. \tag{S55}$$

The triangular receiver basis is divided at its peak into two linear legs. On leg ℓ, its weight is written as $w_\ell(u) = m_\ell u + b_\ell$, where u is the coordinate along that receiver leg. For each source node, let d be the signed receiver-normal offset, let ϑ be the receiver-leg orientation relative to the source, and define

$$R = u^2 + d^2, \qquad \phi = \operatorname{atan2}(u, d). \tag{S56}$$

The first antiderivatives of the receiver-oriented stress kernels are

$$F_{yy} = \frac{1}{2}\sin(2\vartheta)u + \frac{1}{2}d\cos(2\vartheta)\ln R - d\sin(2\vartheta)\phi, \tag{S57}$$

$$F_{xy} = \frac{1}{2}\left[u + d\sin(2\vartheta)\right]\ln R + d\left[1+\cos(2\vartheta)\right]\phi - \cos^2\vartheta\, u, \tag{S58}$$

$$F_\Sigma = u\phi - \frac{1}{2}d\ln R - \vartheta u, \tag{S59}$$

where $\Sigma = xx + yy$ in the source-local frame. To integrate the linear receiver weights analytically, we used second antiderivatives satisfying $\partial\Psi_q/\partial u = F_q$:

$$\begin{aligned}\Psi_{yy} = {} & \frac{1}{2}d\left[u\cos(2\vartheta) + d\sin(2\vartheta)\right]\ln R \\ & + d\left[d\cos(2\vartheta) - u\sin(2\vartheta)\right]\phi + \frac{1}{4}u^2\sin(2\vartheta) - du\cos(2\vartheta),\end{aligned} \tag{S60}$$

$$
\begin{aligned}
\Psi_{xy} = &\left[\frac{1}{4}(u^2 - d^2) + \frac{1}{2}du\sin(2\vartheta) - \frac{1}{2}d^2\cos(2\vartheta)\right]\ln R \\
&+ \left[d^2\sin(2\vartheta) + du\,(1+\cos(2\vartheta))\right]\phi \\
&-u^2\left(\frac{1}{4} + \frac{1}{2}\cos^2\vartheta\right) - du\sin(2\vartheta),
\end{aligned}
\tag{S61}
$$

$$
\Psi_\Sigma = \frac{1}{2}(u^2 - d^2)\phi - \frac{1}{2}du\ln R + \frac{1}{2}du - \frac{1}{2}\vartheta u^2. \tag{S62}
$$

For component $q \in \{yy, xy, \Sigma\}$, the source-node and receiver-leg contributions are assembled as

$$
I_q = \sum_{\ell}\sum_{j=1}^{3}\omega_j\left[(m_\ell u + b_\ell)F_q(u, d_j, \vartheta_\ell) - m_\ell\Psi_q(u, d_j, \vartheta_\ell)\right]_{u_{\ell,1}}^{u_{\ell,2}}. \tag{S63}
$$

With receiver half-length a_r and

$$
K = \frac{\mu A}{2\pi(1-\nu)}, \tag{S64}
$$

the receiver-averaged stresses in the source-local frame are

$$
\overline{\sigma}_{yy}^{\mathrm{CF}} = \frac{K}{a_r}I_{yy}, \qquad \overline{\sigma}_{xy}^{\mathrm{CF}} = -\frac{K}{a_r}I_{xy}, \tag{S65}
$$

$$
\overline{\sigma}_{xx}^{\mathrm{CF}} = \frac{2K}{a_r}I_\Sigma - \overline{\sigma}_{yy}^{\mathrm{CF}}. \tag{S66}
$$

The resulting tensor was rotated from the source-local frame to the global frame using

$$
\overline{\boldsymbol{\sigma}}^{\mathrm{CF}} = \mathbf{Q}\,\overline{\boldsymbol{\sigma}}^{\mathrm{CF},(s)}\mathbf{Q}^{\mathsf{T}}. \tag{S67}
$$

When a receiver crossed the source plane, each receiver leg was split at the crossing before evaluating the endpoint terms. This preserves the branches of $\mathrm{atan2}(u, d)$ without altering the analytical solution.

The independent reference directly integrated the tapered-source stress along the receiver,

$$
\overline{\boldsymbol{\sigma}}^{\mathrm{GL}} = \frac{1}{a_r}\int_{-a_r}^{a_r} N_r(\eta)\,\boldsymbol{\sigma}^{\mathrm{src}}[\mathbf{x}_r(\eta)]\;\mathrm{d}\eta, \qquad N_r(\eta) = 1 - \frac{|\eta|}{a_r}, \tag{S68}
$$

using 600-point Gauss–Legendre quadrature on the same split subintervals. The tensor error was measured with the Frobenius norm,

$$\epsilon_\sigma = \frac{\left\|\overline{\boldsymbol{\sigma}}^{\mathrm{CF}} - \overline{\boldsymbol{\sigma}}^{\mathrm{GL}}\right\|_F}{\left\|\overline{\boldsymbol{\sigma}}^{\mathrm{GL}}\right\|_F}, \tag{S69}$$

or, equivalently in two dimensions,

$$\epsilon_\sigma = \frac{\sqrt{(\Delta\sigma_{xx})^2 + (\Delta\sigma_{yy})^2 + 2(\Delta\sigma_{xy})^2}}{\sqrt{(\sigma_{xx}^{\mathrm{GL}})^2 + (\sigma_{yy}^{\mathrm{GL}})^2 + 2(\sigma_{xy}^{\mathrm{GL}})^2}}. \tag{S70}$$

The benchmark used $L_s = 2a_s = 200$ m, $L_r = 0.8L_s = 160$ m, $A = 1$ m, $\mu = 30$ GPa, and $\nu = 0.25$. Receiver angle ranged from $10°$ to $170°$ at 25 values, the dimensionless receiver-center coordinate along the source ranged from $s = -1.25$ to 1.25 at 31 values, and the dimensionless normal offsets were $h = 0, +0.25, -0.25, +2, -2$. Here s and h are normalized by L_s. The resulting 3875 geometries include intersecting, oblique, offset, and well-separated source–receiver configurations. Across these tests, the median, 99th-percentile, and maximum relative stress-tensor errors were 2.25×10^{-6}, 3.82×10^{-6}, and 1.35×10^{-5}, respectively. Exact coincident self-interactions are treated separately by high-order numerical quadrature in the production calculation and are not included in these geometry maps.

System-level Galerkin BEM and rate-and-state benchmark

We next tested the assembled Galerkin boundary-element and rate-and-state fault-system calculation against the independent DemystiFicatioN_DFN implementation (*57*). This system-level benchmark complements the component-level tests above: Fig. S1 evaluates hydraulic diffusion, Figs. S2 and S3 evaluate the analytical elastic kernels and their Galerkin receiver integration, and Fig. S4 evaluates the resulting fault-cycle and injection-driven response. The two codes were assigned the same fault geometries and discretization, elastic and frictional properties, background stresses, loading velocities, initial conditions, and event-onset criterion. No parameters were adjusted separately to improve agreement between their outputs.

Each benchmark fault was horizontal, 6 km long, and divided into 50 uniform 120-m elements. The elastic medium had shear modulus $\mu = 30$ GPa, Poisson ratio $\nu = 0.25$, and shear-wave speed $V_s = 3\ \mathrm{km\,s^{-1}}$, giving the quasi-dynamic radiation-damping coefficient

$$\eta = \frac{\mu}{2V_s} = 5 \times 10^6 \ \mathrm{Pa\,s\,m^{-1}}. \tag{S71}$$

For this direct cross-code test, both benchmark drivers used the same additive rate-and-state aging formulation,

$$f = f_0 + a \ln\left(\frac{V}{V_0}\right) + b\Phi, \qquad \dot{\Phi} = \frac{V_0 e^{-\Phi} - V}{D_c}, \tag{S72}$$

with quasi-dynamic force balance

$$\tau = \sigma_n' f + \eta V. \tag{S73}$$

The common friction parameters were $f_0 = 0.60$, $V_0 = 10^{-6}\ \mathrm{m\,s^{-1}}$, and $D_c = 0.004$ m. Velocity-weakening regions used $(a, b) = (0.010, 0.014)$, and velocity-strengthening regions used $(a, b) = (0.020, 0.010)$. Where a tip transition was prescribed, its characteristic length was $L_{\mathrm{tip}} = 0.1L_f = 600$ m and its smoothing width was $L_{\mathrm{tip}}/3 = 200$ m. Defining d as distance from the relevant fault tip, the interpolation weight was

$$w(d) = \frac{1}{2}\left[\tanh\left(\frac{d - L_{\mathrm{tip}}}{L_{\mathrm{tip}}/3}\right) + 1\right], \tag{S74}$$

with $a = a_{\mathrm{VS}}(1-w) + a_{\mathrm{VW}}w$ and the same interpolation for b. The recurrent single-fault test used this transition at one end of the fault, matching the corresponding reference configuration. In the parallel-fault test, Fault 1 had symmetric velocity-strengthening tip transitions and a velocity-weakening interior, whereas Fault 2 was velocity strengthening along its full length. The injection-driven test used symmetric tip transitions.

The background stress tensor had $S_{H\,\max} = 90$ MPa, $S_{h\,\min} = 46$ MPa, and $S_{H\,\max}$ azimuth 73°. Its resolution onto the horizontal benchmark faults gave $\tau_0 = 12.3022$ MPa and total normal stress $\sigma_{n,0} = 49.7612$ MPa. With background pore pressure $P_0 = 28.9$ MPa and $\alpha = 1$, the initial effective normal stress was $\sigma_{n,0}' = 20.8612$ MPa. Slip-mediated elastic stress changes were calculated from the assembled Galerkin matrices K_s and K_n, and no slip-induced poroelastic pressure feedback was included in this benchmark. Thus,

$$\dot{\tau} = K_s(V - V_{\mathrm{pl}}), \qquad \sigma_n' = \sigma_{n,0} + K_n\delta - \alpha(P_0 + P), \tag{S75}$$

and the logarithmic-velocity evolution used in the present Galerkin BEM calculation was

$$\frac{d\ln V}{dt} = \frac{K_s(V - V_{\rm pl}) - f\left(K_n V - \alpha \dot{P}\right) - \sigma_n' b\dot{\Phi}}{\eta V + a\sigma_n'}. \tag{S76}$$

Initial slip was zero, $\Phi_0 = \ln(V_0/V_{\rm pl})$, and the initial velocity of every element was obtained by solving the quasi-dynamic force-balance equation. The no-injection single- and parallel-fault tests used $V_{\rm pl} = 10^{-9}$ m s^{-1} and were integrated for 100 years. The injection-driven test used $V_{\rm pl} = 10^{-11}$ m s^{-1}, a 70-year mechanical spin-up without injection, and 30 years of subsequent central injection. In all three tests, an event began when the maximum slip velocity on a fault first crossed 10^{-3} m s^{-1}. This threshold is specific to the cross-code benchmark and is distinct from the 10^{-2} m s^{-1} dynamic-rupture threshold used to classify the Prague simulations.

For the injection-driven test, DemystiFicatioN_DFN solved the one-dimensional pressure equation natively on the same 50 control volumes. The hydraulic parameters were diffusivity $D = 0.1$ m^2 s^{-1}, permeability $k = 10^{-13}$ m^2, porosity $\phi = 0.1$, fluid viscosity $\mu_f = 10^{-3}$ Pa s, fluid compressibility $\beta_f = 9 \times 10^{-9}$ Pa^{-1}, and pore-volume compressibility $\beta_\phi = 10^{-9}$ Pa^{-1}. A constant total one-dimensional source rate $Q = 5 \times 10^{-8}$ m s^{-1} was split equally between the two central control volumes and maintained for 30 years. To isolate the system-level mechanical comparison from differences between hydraulic solvers, the resulting element-wise $P(x,t)$ and $\dot{P}(x,t)$ histories were supplied to the Galerkin BEM calculation by linear interpolation. The Galerkin calculation was integrated with Matlab `ode15s` using relative tolerance 10^{-5}, absolute tolerance 10^{-7}, maximum step 3×10^7 s, and initial step 10^{-3} s. Off-diagonal Galerkin interactions were evaluated with the analytical kernel verified in Fig. S3, whereas coincident self-interactions used 600-point Gauss–Legendre quadrature. The DemystiFicatioN_DFN benchmark drivers were compiled against repository revision `536eb7297cbc65208f2b14497089bf0864c42dc2` and used an adaptive embedded Runge–Kutta scheme with relative tolerance 10^{-5}, absolute tolerance 10^{-8}, initial step 0.01 year, and maximum step 0.1 year. Table S6 collects the parameters needed to reproduce the three tests.

The single-fault calculations produced 12 events in both codes (Fig. S4B). The first-event times were 5.56 and 5.28 years, and the mean recurrence intervals were 8.48 and 8.01 years, for the Galerkin BEM and DemystiFicatioN_DFN, respectively. Their final fault-mean slips differed by 4.24%. In the parallel-fault test, the active Fault 1 produced 13 and 14 events, with mean recurrence intervals of 7.15 and 6.74 years. Fault 2 remained below the event threshold in both calculations. At 100 years, the differences in fault-mean cumulative slip were 0.79% for Fault 1 and 0.64% for Fault 2 (Fig. S4C). In the injection test, rupture began 4.56997 and 4.57990 years after injection onset, a difference of 0.00993 year (3.63 days), or 0.217% of the reference onset time (Fig. S4D). The peak slip velocities were 0.406 and 0.374 $\mathrm{m\,s^{-1}}$. These tests show that the two independent implementations reproduce the same recurrent, interacting-fault, and injection-driven behaviors under matched inputs, with small quantitative differences arising from their distinct spatial kernels and time-integration implementations.

Spatiotemporal evolution of the calibrated Prague cascade

To document the space-time rupture kinematics underlying the event timing, magnitude, and rupture-length metrics in Figure 2C, we evaluated the modeled slip velocity $V_i(t)$ along each of the three primary faults from injection onset through model year 30 (Fig. S5). The three panels use the same monotonic nonlinear time coordinate. This common mapping retains the full injection-to-nucleation history while expanding the short interval containing the three dynamic ruptures, allowing their spatial evolution to be resolved on the same ordinate. The annotated values give the corresponding physical rupture times.

Dynamic rupture onset on each fault was defined as the first time any of its elements crossed $V_{\mathrm{dyn}} = 10^{-2}\ \mathrm{m\,s^{-1}}$. Fault 1 reached this threshold 17.96 years after injection onset. Fault 2 followed 0.96 day after Fault 1, and Fault 3 followed 1.95 days after Fault 2, or 2.91 days after Fault 1. The velocity fields additionally show the along-fault propagation and spatial extent of slip during each event.

Event 2 normal-stress loading of Fault 3

To separate the competing mechanical effects of Event 2 on Fault 3, we isolated the slip accumulated during the modeled Fault 2 dynamic rupture and evaluated its elastic stress transfer to Fault 3. Event 2 increased shear stress in the modeled slip direction of Fault 3, as shown in Figure 2D, but also increased compressive total normal stress along the entire fault. The latter contribution clamps Fault 3 and inhibits slip. The local fault-zone pore-pressure response is represented as offsetting a fraction β_{eff} of this total-normal-stress increase, giving the residual effective-normal-stress change

$$\Delta\sigma'_{n,\text{slip}} = (1 - \beta_{\text{eff}})\Delta\sigma_{n,\text{slip}}. \tag{S77}$$

Here compression is positive. Increasing β_{eff} reduces the effective-normal-stress clamping without altering the Event 2 shear-stress transfer. Figure S6 shows this reduction across Fault 3, including the coupling interval over which the modeled Fault 3 response changes from nondynamic to dynamic rupture in Figure 3A.

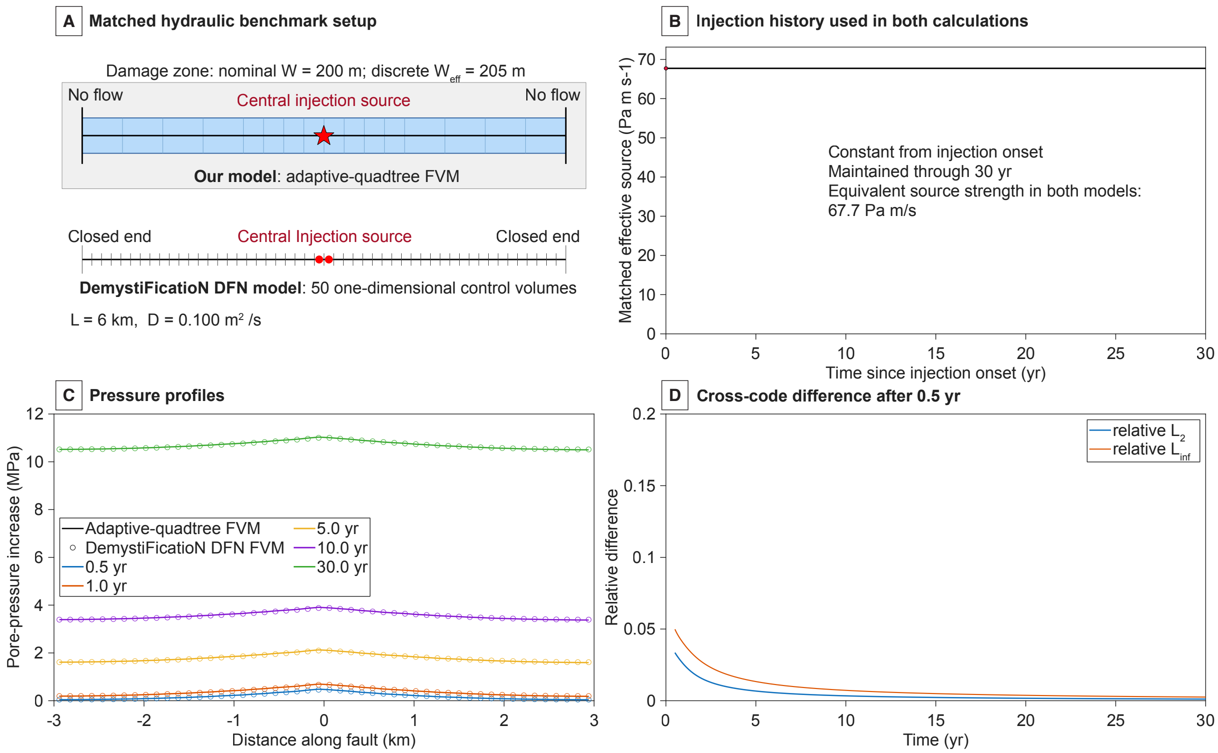

Figure S1: **Hydraulic diffusion benchmark against** DEMYSTIFICATION_DFN. (**A**) Matched geometry and boundary conditions. The adaptive-quadtree model represents a nominally 200-m-wide damage zone with a discrete effective width of 205 m, whereas the DEMYSTIFICATION_DFN model represents the same 6-km fault with 50 one-dimensional control volumes. Both models use a central source and closed or effectively no-flow ends. (**B**) Constant 30-year injection history. The raw source-rate parameters differ between the two formulations, but their effective line-source strengths are both 67.7 $\mathrm{Pa\,m\,s^{-1}}$. (**C**) Pressure profiles at 0.5, 1, 5, 10, and 30 years. Solid lines show the adaptive-quadtree solution, and open circles show the DEMYSTIFICATION_DFN solution. (**D**) Time-dependent relative L_2 and L_∞ differences from 0.5 to 30 years. The global relative L_2 difference over all stored pressure fields is 0.00193.

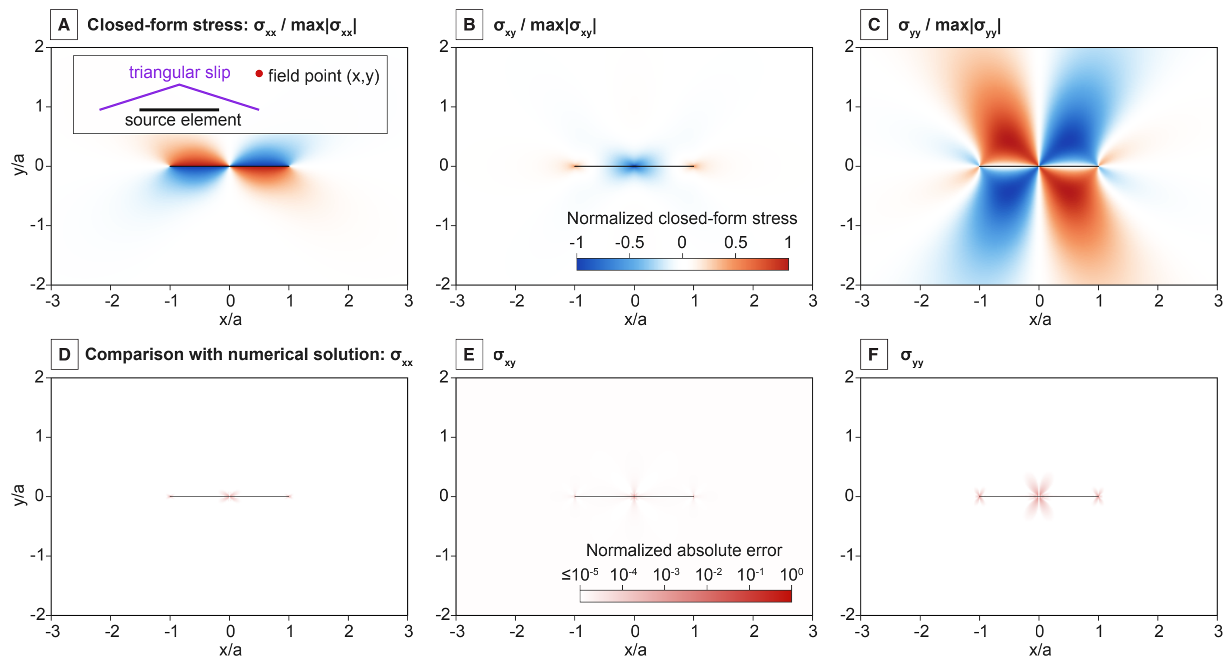

Figure S2: **Closed-form tapered-source stress kernel benchmark.** (**A–C**) Closed-form σ_{xx}, σ_{xy}, and σ_{yy} generated by a triangular slip basis associated with a horizontal source element. Each component is normalized by the maximum absolute value of the corresponding Fourier-domain solution. The inset in (**A**) illustrates the discrete source element, the triangular basis whose support is twice the element length, and a generic field point. (**D–F**) Normalized absolute differences between the closed-form and Fourier-domain solutions for the same three components. The white-to-red logarithmic scale is common to all three panels; white denotes $\epsilon_{ij} \leq 10^{-5}$. The thin horizontal line identifies the support of the triangular source basis. The field-point grid is staggered about the source plane and does not sample the singular line itself.

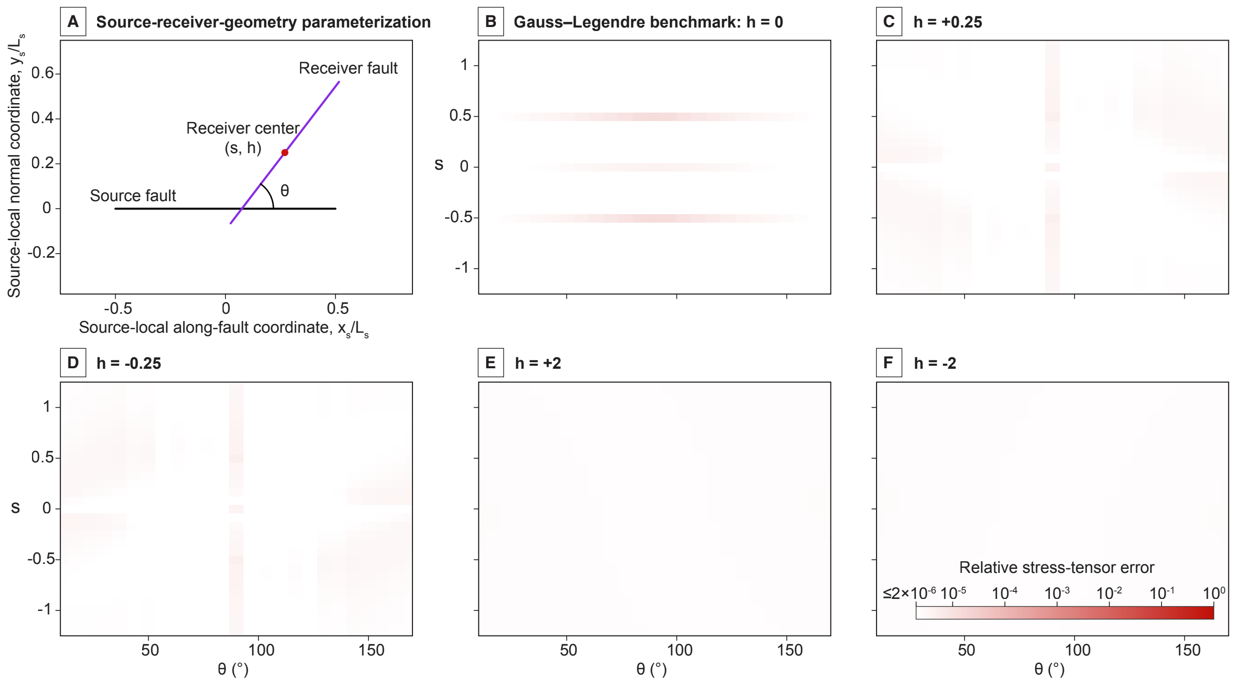

Figure S3: **Closed-form Galerkin source-to-receiver interaction benchmark.** (**A**) Source–receiver geometry parameterization. The source-local coordinate system is centered at the source midpoint, with its horizontal axis parallel to the source and its normal axis perpendicular to the source. The dimensionless receiver-center coordinates (s, h) are normalized by source length L_s, θ is the receiver angle relative to the source, and $L_r/L_s = 0.8$. (**B–F**) Relative stress-tensor error between the closed-form Galerkin interaction and 600-point Gauss–Legendre quadrature as a function of s and θ, for $h = 0, +0.25, -0.25, +2$, and -2, respectively. The common white-to-red logarithmic scale emphasizes departures from the numerical reference; white denotes $\epsilon_\sigma \leq 2 \times 10^{-6}$. The comparison spans 3875 source–receiver geometries, including intersecting and nonintersecting configurations.

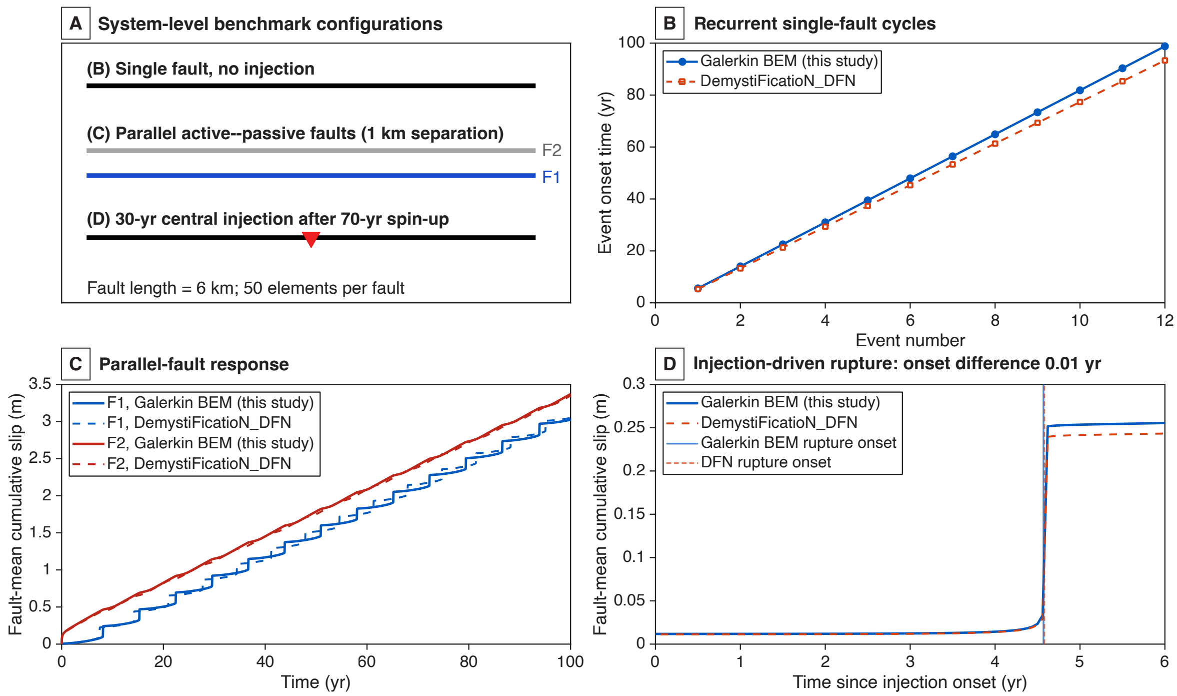

Figure S4: **System-level Galerkin BEM and rate-and-state benchmark against DEMYSTIFICATION_DFN.** (**A**) The three matched configurations: a single fault without injection, two parallel faults separated by 1 km with seismogenic Fault 1 and velocity-strengthening Fault 2, and a centrally injected single fault following a 70-year mechanical spin-up. Every fault is 6 km long and discretized into 50 elements. (**B**) Event-onset time versus event number during 100 years of recurrent single-fault cycles without injection. Events are defined by the first crossing of $V_{\max} = 10^{-3}\ \mathrm{m\,s^{-1}}$. (**C**) Fault-mean cumulative slip on the active Fault 1 and passive Fault 2 in the parallel-fault test. Solid lines show the Galerkin BEM calculation from this study, and dashed lines show DEMYSTIFICATION_DFN. (**D**) Fault-mean cumulative slip during the first six years after injection onset. Both mechanical calculations use the same element-wise pressure and pressure-rate histories generated by the native DEMYSTIFICATION_DFN diffusion solver. Vertical lines mark rupture onset; the two onset times differ by 0.00993 year (3.63 days).

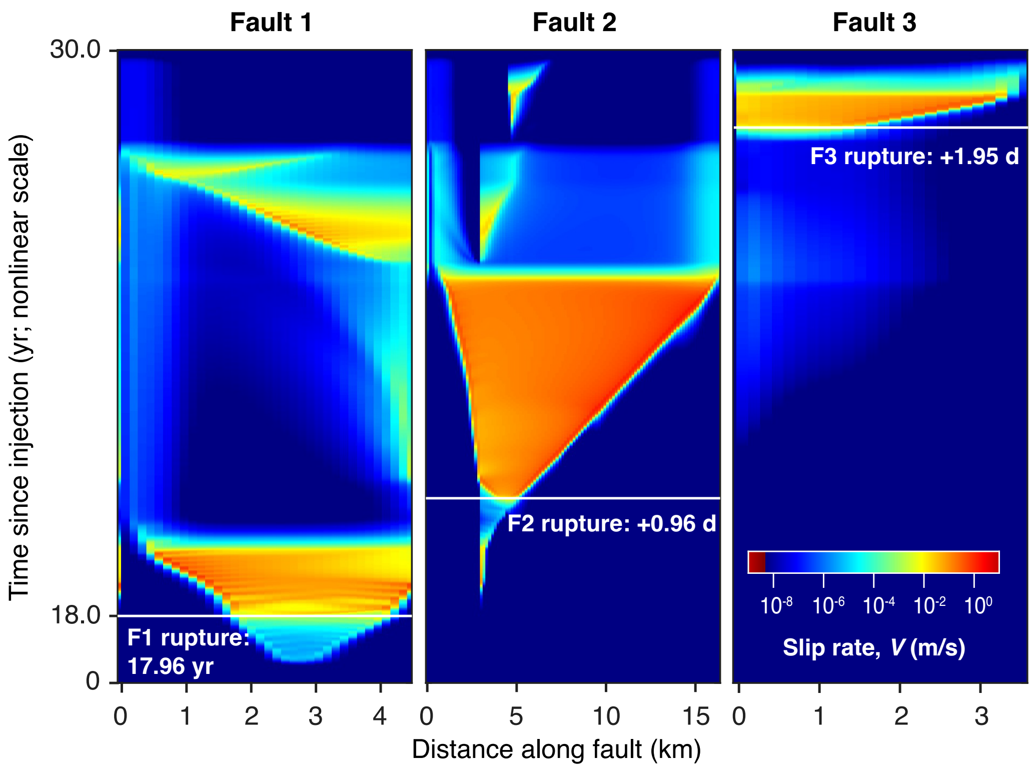

Figure S5: **Spatiotemporal evolution of the modeled Prague fault cascade.** Slip rate V along Faults 1–3 from injection onset through model year 30. Color denotes slip rate on a logarithmic scale from 10^{-8} to 10^{0} $\mathrm{m\,s^{-1}}$. All three panels share the same monotonic nonlinear time coordinate, which expands the short interval containing the three dynamic ruptures while retaining the complete 30-year evolution. White horizontal lines mark dynamic rupture onset, defined by the first crossing of $V = 10^{-2}$ $\mathrm{m\,s^{-1}}$ on each fault. Fault 1 ruptures 17.96 years after injection onset; the annotated Fault 2 and Fault 3 delays are measured relative to rupture onset on the immediately preceding fault. Fault 3 therefore ruptures 2.91 days after Fault 1.

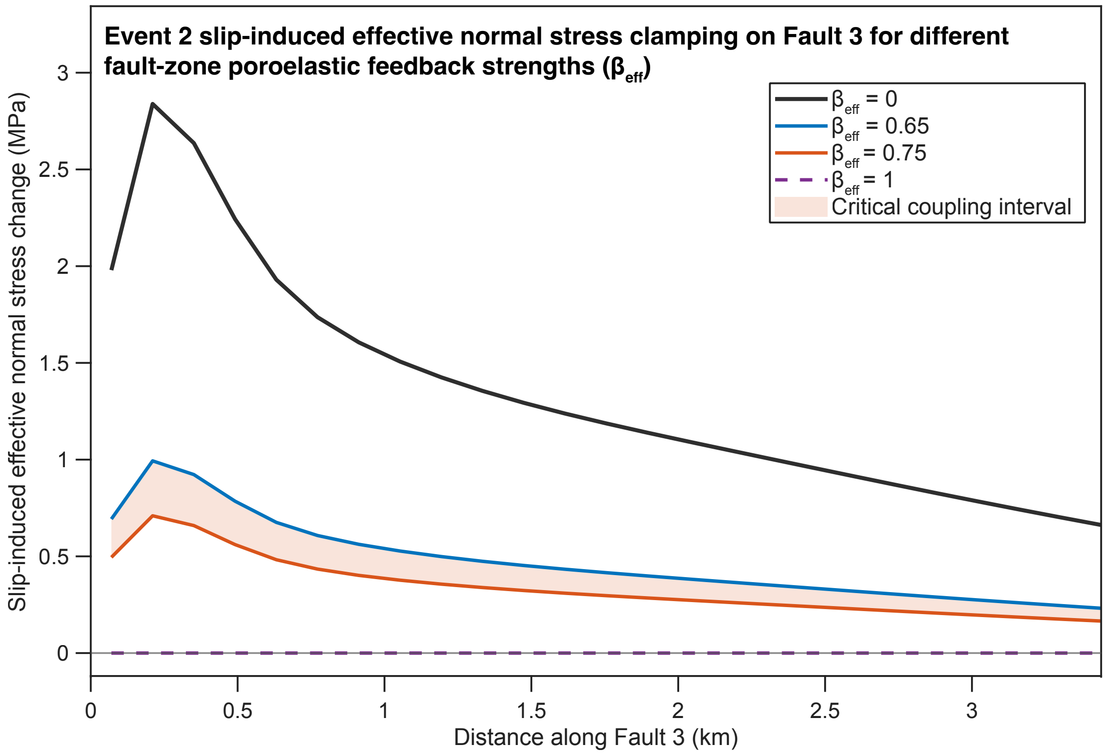

Figure S6: **Event 2 slip-induced effective-normal-stress clamping on Fault 3 for different fault-zone poroelastic feedback strengths.** The source slip is isolated to the modeled Fault 2 dynamic rupture, and distance is measured along Fault 3. Compression is positive. The $\beta_{\text{eff}} = 0$ curve shows the slip-induced total-normal-stress increase, which is fully expressed as an effective-normal-stress increase when no local pore-pressure feedback is included. For nonzero β_{eff}, the plotted residual effective-normal-stress clamping is $(1 - \beta_{\text{eff}})\Delta\sigma_{n,\text{slip}}$. The shaded region spans the residual clamping between $\beta_{\text{eff}} = 0.65$ and 0.75, which brackets the transition to dynamic Fault 3 rupture identified in Figure 3A. At $\beta_{\text{eff}} = 1$, the local pore-pressure response completely buffers this normal-stress contribution. The favorable Event 2 shear-stress loading of Fault 3 is unchanged by β_{eff} and is shown in Figure 2D.

Table S1: **Exact fault geometries used in the Prague simulations.** (**A**) Three-fault configuration used in Figures 2–4. (**B**) Extended 27-fault configuration used in Figure 5. Coordinates are reported in the local east–north Cartesian system, and N_e is the number of uniformly spaced elements on each segment. **(A) Three-fault configuration used in Figures 2–4**

Fault ID	Start point (x_1, y_1) (m)	End point (x_2, y_2) (m)	N_e
1	$(6720, 7070)$	$(4520, 3240)$	35
2	$(6790, 4860)$	$(-6420, -4700)$	105
3	$(3210, 2270)$	$(-300, 2270)$	25

Table S1: **Exact fault geometries used in the Prague simulations.** (continued). **(B) Extended 27-fault configuration used in Figure 5**

Fault ID	Start point (x_1, y_1) (m)	End point (x_2, y_2) (m)	N_e
1	$(6626.8, 7226.8)$	$(4980.9, 3546.8)$	27
2	$(4980.9, 3546.8)$	$(-6420.0, -4700.0)$	90
3	$(3210.0, 2270.0)$	$(-300.0, 2270.0)$	25
4	$(8704.5, 11068.6)$	$(8353.7, 10581.7)$	5
5	$(8353.7, 10581.7)$	$(7895.0, 9743.0)$	7
6	$(7895.0, 9743.0)$	$(6303.1, 7443.9)$	19
7	$(6303.1, 7443.9)$	$(5736.4, 7201.0)$	5
8	$(5736.4, 7201.0)$	$(5385.7, 6633.0)$	5
9	$(5385.7, 6633.0)$	$(5736.4, 6009.7)$	5
10	$(5736.4, 6009.7)$	$(3982.6, 2356.9)$	28
11	$(8508.9, 11082.4)$	$(8299.7, 10500.6)$	5
12	$(7922.0, 8714.1)$	$(6303.1, 7443.9)$	14
13	$(6357.0, 6577.3)$	$(5736.4, 6009.7)$	6
14	$(7733.1, 7089.7)$	$(6222.1, 6144.3)$	12
15	$(7679.2, 6521.2)$	$(6950.6, 5303.9)$	10
16	$(6950.6, 5303.9)$	$(6087.2, 3978.4)$	11
17	$(4980.9, 3546.8)$	$(6330.0, 4059.3)$	10
18	$(6384.0, 4167.5)$	$(6087.2, 3328.5)$	6
19	$(6087.2, 3328.5)$	$(5385.7, 1732.1)$	12
20	$(5385.7, 1732.1)$	$(4549.2, -270.3)$	15
21	$(4549.2, -270.3)$	$(3065.2, -2326.0)$	17
22	$(3065.2, -2326.0)$	$(2066.8, -3515.8)$	11
23	$(2066.8, -3515.8)$	$(-64.8, -7980.3)$	33
24	$(6249.1, 3761.5)$	$(4792.1, 2220.3)$	15
25	$(4792.1, 2220.3)$	$(3793.7, 245.2)$	15
26	$(4252.4, -26.2)$	$(3523.9, -756.2)$	7
27	$(3523.9, -756.2)$	$(3038.2, -2325.9)$	11

Table S2: **Fault-wide shear-stress adjustments and sequence-response metrics.** Each listed adjustment was applied uniformly to all elements of the corresponding fault while preserving the along-fault stress heterogeneity inherited from long-term fault-system evolution. (**A**) Best-matching simulation at each effective fault-zone poroelastic coupling used in Figures 3A–C. The $\beta_{\text{eff}} = 1$ row is also the Figure 2 reference prestress used without retuning in Figure 3D and Figure 4. Fault 1 nucleated after approximately 18 years and Fault 2 followed after approximately one day in all retained simulations. The reported Fault 2–Fault 3 response delay refers to the principal Fault 3 response, which was slow-slip-like at $\beta_{\text{eff}} = 0.25$–$0.65$ and dynamic at $\beta_{\text{eff}} \geq 0.75$. An em dash in the response-delay column indicates that no corresponding Fault 3 response was identified; an em dash in the magnitude tuple indicates that Fault 3 did not rupture dynamically. (**B**) Separately calibrated Faults 1–3 shear-stress adjustments for each receiver-fault prestress offset in Figure 5. All six simulations satisfied the prescribed timing intervals and rupture order. **(A) Three-fault effective-coupling experiments**

β_{eff}	Faults 1–3 shear-stress adjustments $(\Delta\tau_1, \Delta\tau_2, \Delta\tau_3)$ (MPa)	Fault 1–Fault 2 event delay (d)	Fault 2–Fault 3 response delay (d)	$V_{\max,3}$ (m s^{-1})	$(M_{w,1}, M_{w,2}, M_{w,3})$
0	$(-0.015, -0.331, +0.212)$	1	—	2×10^{-9}	$(4.9, 5.5, —)$
0.25	$(-0.015, -0.230, +0.213)$	1	23	5×10^{-7}	$(4.9, 5.6, —)$
0.50	$(-0.015, -0.145, +0.212)$	1	12	1×10^{-4}	$(4.9, 5.6, —)$
0.65	$(-0.015, -0.090, +0.213)$	1	3	7×10^{-3}	$(4.9, 5.7, —)$
0.75	$(-0.015, -0.060, +0.212)$	1	2	2×10^{-2}	$(4.9, 5.7, 4.4)$

Table S2: **Fault-wide shear-stress adjustments and sequence-response metrics.** (continued). **(A) Three-fault effective-coupling experiments**

β_{eff}	Faults 1–3 shear-stress adjustments $(\Delta\tau_1, \Delta\tau_2, \Delta\tau_3)$ (MPa)	Fault 1–Fault 2 event delay (d)	Fault 2–Fault 3 response delay (d)	$V_{\text{max},3}$ (m s^{-1})	$(M_{w,1}, M_{w,2}, M_{w,3})$
0.85	$(-0.015, -0.030, +0.210)$	1	2	4×10^{-2}	$(4.9, 5.7, 4.6)$
0.90	$(-0.015, -0.020, +0.208)$	1	2	5×10^{-2}	$(4.9, 5.7, 4.7)$
1.00	$(-0.015, +0.003, +0.204)$	1	2	6×10^{-2}	$(4.9, 5.7, 4.8)$

Table S2: **Fault-wide shear-stress adjustments and sequence-response metrics.** (continued). **(B) Post-sequence fault-network prestress experiments**

Receiver-fault prestress offset (MPa)	Faults 1–3 shear-stress adjustments $(\Delta\tau_1, \Delta\tau_2, \Delta\tau_3)$ (MPa)	Fault 1 rupture time (yr)	Fault 1–Fault 2 event delay (d)	Fault 2–Fault 3 event delay (d)	Rupture order	$(M_{w,1}, M_{w,2}, M_{w,3})$
0 (long-term mean)	(+0.121000, +0.081500, +0.004500)	17.789	1.104	2.388	1–2–3	(4.86, 5.66, 4.75)
+0.1	(+0.113000, +0.079951, +0.005075)	17.892	0.834	2.027	1–2–3	(4.86, 5.66, 4.72)
+0.2	(+0.102000, +0.078373, +0.005098)	17.899	1.193	2.198	1–2–3	(4.82, 5.66, 4.76)
+0.3	(+0.090000, +0.076868, +0.007380)	17.807	0.815	1.818	1–2–3	(4.80, 5.66, 4.76)
+0.4	(+0.075200, +0.074417, +0.008560)	17.965	1.162	2.327	1–2–3	(4.72, 5.65, 4.77)
+0.5	(+0.075750, +0.072626, +0.014140)	17.734	0.818	2.318	1–2–3	(4.67, 5.65, 4.76)

Table S3: **Master model parameters.** Values are common to the three-fault and 27-fault calculations unless separate entries are given. The hydraulic table reports diffusivity directly because this is the governing transport parameter varied in the experiments. The Biot coefficient derived from the hydraulic-solver material parameters is distinguished from the effective-pressure coefficient used in the fault-dynamics calculation. **(A) Mechanical, frictional, and numerical parameters**

Parameter	Symbol	Three-fault model (Figures 2–4)	27-fault model (Figure 5)
Number of faults	—	3	27
Number of boundary elements	N	165	426
Shear modulus	μ	30 GPa	30 GPa
Poisson ratio	ν	0.25	0.25
Shear-wave speed	V_s	3 km s^{-1}	3 km s^{-1}
Radiation-damping coefficient	$\eta = \mu/(2V_s)$	5×10^6 Pa s m^{-1}	Same
Reference friction coefficient	f_0	0.60	0.60
Reference slip velocity	V_0	10^{-6} m s^{-1}	Same
Velocity-weakening parameters	(a, b)	$(0.005, 0.007)$	Same
Velocity-strengthening tip parameters	(a, b)	$(0.010, 0.005)$	Same
Tip-transition implementation	—	10% of fault length, capped at 1 km, at designated outer tips	500 m at terminal network tips identified using a 150-m endpoint-attachment tolerance

Table S3: **Master model parameters.** (continued). **(A) Mechanical, frictional, and numerical parameters**

Parameter	Symbol	Three-fault model (Figures 2–4)	27-fault model (Figure 5)
Tip-transition smoothing	—	Hyperbolic-tangent interpolation with smoothing width $L_{\mathrm{tip}}/3$	Same
State-evolution distance	L	0.002 m	Same
Background pore pressure	P_0	30 MPa	Same
Effective-pressure coefficient in fault dynamics	α	1	1
Reference effective fault-zone coupling	β_{eff}	1 in Figure 2	1
Element-activation threshold	V_{act}	10^{-4} m s^{-1}	Same
Dynamic-rupture threshold	V_{dyn}	10^{-2} m s^{-1}	Same
Rupture-length slip cutoff	D_{cut}	0.01 m	Same
Out-of-plane seismogenic width	W	3.5 km	3.5 km
Fault-dynamics integrator	—	MATLAB `ode15s`	Same
Relative/absolute ODE tolerances	—	$10^{-5}/10^{-7}$	Same
Maximum ODE step	—	3×10^7 s	Same

Table S3: **Master model parameters.** (continued). **(B) Background stress and prestress initialization**

Parameter	Three-fault model (Figures 2–4)	27-fault model (Figure 5)
$S_{H\,\max}$ azimuth	73° clockwise from north	Same
$(S_{H\,\max}, S_{h\,\min})$	$(90, 46)$ MPa	Same
Long-term evolution interval	5000 yr	3000 yr
Prestress-template time	4300 yr	2930 yr
Mean long-term loading velocity	10^{-11} m s^{-1}	10^{-11} m s^{-1}
Element-wise loading-velocity range in the retained model	8.15×10^{-12}–1.45×10^{-11} m s^{-1}	1.63×10^{-12}–1.24×10^{-11} m s^{-1}
Active loading during injection and post-injection calculations	$V_L = 0$	$V_L = 0$
Fault-wide prestress treatment	Faults 1–3 adjusted as listed in Table S2A	Faults 4–27 assigned a common offset from their individual long-term means; Faults 1–3 adjusted separately for each simulation as listed in Table S2B
Receiver-fault prestress offsets	—	0, +0.1, +0.2, +0.3, +0.4, and +0.5 MPa

Table S3: **Master model parameters.** (continued). **(C) Hydraulic and poroelastic parameters**

Parameter	Value
Hydraulic-solver Lamé parameters	$\lambda = \mu = 30$ GPa
Grain/fluid bulk moduli	$K_s = 100$ GPa; $K_f = 2.25$ GPa
Porosity	$\phi = 0.01$
Fluid viscosity	$\mu_f = 0.4$ mPa s
Biot coefficient derived in the hydraulic solver	$\alpha_h = 0.50$
Skempton coefficient derived in the hydraulic solver	$B_h = 0.697$
Composite hydraulic coefficient	$\mathcal{C}_h \approx 4.8 \times 10^{-15}$ s
Reference host-rock permeability	$k_{\mathrm{bg}} \approx 8.4 \times 10^{-18}$ m^2
Reference background diffusivity in Figs. 2, 4, and 5	$D_{\mathrm{bg}} = 1.74 \times 10^{-3}$ m^2 s^{-1}
Reference fault-damage-zone diffusivity in Figs. 2, 4, and 5	$D_{\mathrm{dz}} = 1.74$ m^2 s^{-1} $= 1000 D_{\mathrm{bg}}$
Hydraulic domain	25.6×25.6 km
Quadtree refinement levels/cell widths	Levels 5–9; cell widths 800–50 m
Damage-zone half-width in the finite-volume grid	100 m
Initial pressure perturbation	0
Reference two-dimensional source rate	$q_{\mathrm{ref}} \approx 1.7 \times 10^{-7}$ m^2 s^{-1}
Effective out-of-plane flow thickness	$h_{\mathrm{eff}} \approx 1.78$ km
Reference injection-source coordinates	$(x, y) = (6400, 6800)$ m
Extraction-source coordinates in Figure 4D	$(x, y) = (5620, 5160)$ m
Source ramp	30 days, except in the square-wave intermittent experiments

Table S3: **Master model parameters.** (continued). **(C) Hydraulic and poroelastic parameters**

Parameter	Value
External hydraulic boundary condition	Zero normal flux
Pressure integrator	Implicit Crank–Nicolson with reused sparse LU factorization
Reference 100-year pressure histories, including Figure 5	2000 uniform time steps (20 steps yr^{-1})
Figure 4C intermittent pressure histories	6000 uniform steps over 100 yr (60 steps yr^{-1}); 20,000 steps for the $T_r = 3$ d cases (200 steps yr^{-1})

Table S3: **Master model parameters.** (continued). **(D) Regional-stress-resolved initial conditions for the three-fault long-term calculation**

Fault	τ_0 (MPa)	$\sigma_{n,0}$ (MPa)	$\sigma'_{n,0}$ (MPa)	$\tau_0/\sigma'_{n,0}$	V_L (m s^{-1})	Φ_0
Fault 1	21.953	66.562	36.562	0.600	1.454×10^{-11}	11.139
Fault 2	13.480	50.613	20.613	0.654	8.928×10^{-12}	11.626
Fault 3	12.302	49.761	19.761	0.623	8.148×10^{-12}	11.718

Table S4: **Exact parameter grids and operational schedules used in Figs. 3–5.** Unless otherwise stated, the experiments used the reference mechanical, frictional, hydraulic, and prestress parameters in Table S3, the reference injection source at $(x, y) = (6400, 6800)$ m, $q_{2D} = q_{ref}$, and $V_L = 0$. Here $q_{ref} \approx 1.7 \times 10^{-7}$ m^2 s^{-1} is the reference two-dimensional source rate. Source rates are expressed relative to q_{ref}; diffusivity values are rounded to three significant figures. The source coordinates use the same local east–north Cartesian system as Table S1. **(A) Effective fault-zone coupling experiments (Figures 3A–C)**

Varied parameter	Values	Prestress treatment	Injection schedule
β_{eff}	0, 0.25, 0.50, 0.65, 0.75, 0.85, 0.90, 1.00	Faults 1–3 adjusted separately at each value; best-matching simulation retained (Table S2A)	Reference rate maintained for the duration of each calculation

Table S4: **Exact parameter grids and operational schedules used in Figs. 3–5.** (continued). **(B) Hydraulic-diffusivity experiments (Figure 3D)**

Fault-damage-zone diffusivity, D_{dz} (m^2 s^{-1})	Tested host-rock diffusivities, D_{bg} (m^2 s^{-1})
1.74×10^{-4}	1.74×10^{-4}
1.74×10^{-3}	1.74×10^{-4},5.49×10^{-4},1.74×10^{-3}
1.74×10^{-2}	1.74×10^{-4},5.49×10^{-4},1.74×10^{-3},5.49×10^{-3},1.74×10^{-2}
1.74×10^{-1}	1.74×10^{-4},5.49×10^{-4},1.74×10^{-3},5.49×10^{-3},1.74×10^{-2}
1.74	1.74×10^{-4},5.49×10^{-4},1.74×10^{-3},5.49×10^{-3},1.74×10^{-2}
17.4	1.74×10^{-4},5.49×10^{-4},1.74×10^{-3},5.49×10^{-3},1.74×10^{-2}

Table S4: **Exact parameter grids and operational schedules used in Figs. 3–5.** (continued). **(C) Source-distance experiments (Figure 4A)**

Relative-distance factor	Source–fault distance (km)	Source x (m)	Source y (m)	Continuous schedule	Finite-duration schedule
0.5	0.07150	6462.00	6764.39	Injection maintained to first nucleation	18 yr injection, followed where necessary by shut-in evolution to first nucleation
1	0.14300	6400.00	6800.00	Same	Same
2	0.28599	6276.00	6871.22	Same	Same
4	0.57199	6028.01	7013.67	Same	Same
8	1.14397	5532.03	7298.57	Same	Same
16	2.28795	4540.06	7868.37	Same	Same
32	4.57589	2556.12	9007.97	Same	Same
64	9.15178	−1411.76	11287.17	Same	Same

Table S4: **Exact parameter grids and operational schedules used in Figs. 3–5.** (continued). **(D) Steady-rate and intermittent-injection experiments (Figs. 4B and 4C)**

Experiment	Injection-on interval, T_g (d)	Shut-in intervals, T_r (d)	Relative peak rate, $q_{\text{peak}}/q_{\text{ref}}$	Relative cycle-averaged rate, $q_{\text{avg}}/q_{\text{ref}}$	Duration
Steady-rate sweep (Figure 4B)	Continuous	0	0.03, 0.1, 0.3, 1, 3, 10, 30	Equal to relative peak rate	To first nucleation
Fixed-peak intermittency (Figure 4C)	30	0, 3, 7, 15, 30, 60	1 for every T_r	$T_g/(T_g+T_r)$	Repeated to first nucleation
Fixed-average intermittency (Figure 4C)	30	0, 3, 7, 15, 30, 60	$(T_g+T_r)/T_g$	1	Repeated to first nucleation

Table S4: **Exact parameter grids and operational schedules used in Figs. 3–5.** (continued). **(E) Injection–extraction experiments (Figure 4D)**

Parameter	Values
Injection-source coordinates	$(6400, 6800)$ m
Extraction-source coordinates	$(5620, 5160)$ m
Injection rate	$q_{\text{inj}} = q_{\text{ref}}$
Extraction-to-injection ratio, $q_{\text{ext}}/q_{\text{inj}}$	0, 0.25, 0.50, 0.75, 0.80, 0.90
Relative net source rate, $(q_{\text{inj}} - q_{\text{ext}})/q_{\text{ref}}$	1, 0.75, 0.50, 0.25, 0.20, 0.10
Duration	Injection and extraction maintained to first nucleation

Table S4: **Exact parameter grids and operational schedules used in Figs. 3–5.** (continued). **(F) Post-sequence fault-network prestress experiments (Figure 5)**

Parameter	Values or treatment
Receiver faults	Faults 4–27
Common receiver-fault prestress offset	0, +0.1, +0.2, +0.3, +0.4, +0.5 MPa relative to the long-term mean shear stress of each fault
Faults 1–3 prestress treatment	Shear-stress adjustments determined separately for each receiver-fault simulation (Table S2B)
Effective fault-zone coupling	$\beta_{\text{eff}} = 1$
Injection schedule	Reference source and rate from model year 0 to year 19, including a 30-day startup ramp; $q_{2D} = 0$ thereafter
Active long-term loading	$V_L = 0$ throughout injection and post-injection evolution
Primary-sequence constraints	Fault 1 rupture at 17.5–18.0 yr; Fault 1–Fault 2 delay 0.8–1.2 d; Fault 2–Fault 3 delay 1.8–2.5 d; rupture order 1–2–3; all three faults dynamically rupturing
Receiver-response window	End of the reproduced Prague sequence to model year 100

Table S5: **Matched parameters for the hydraulic diffusion benchmark in Fig. S1.** The two formulations use different constitutive storage and source-rate parameters; the hydraulic diffusivity and effective line-source strength were matched directly.

Quantity	Adaptive-quadtree FVM	DemystiFicatioN_DFN FVM
Geometry	6-km horizontal damage zone in a two-dimensional quadtree domain	6-km one-dimensional fault
Fault sampling/discretization	50 uniformly spaced fault elements	50 uniform control volumes, 120 m each
Damage-zone width	Nominal $W = 200$ m; discrete $W_{\text{eff}} = 205$ m	One-dimensional representation
End condition	Effectively no flow owing to negligible background diffusivity and no-flux outer boundaries	Closed/no flow
Hydraulic diffusivity D	9.9956×10^{-2} m^2 s^{-1}	9.9956×10^{-2} m^2 s^{-1}
Hydraulic/storage parameters	$\lambda = \mu = 30$ GPa; $K_s = 100$ GPa; $K_f = 2.25$ GPa; $\phi = 0.01$; $\mu_f = 0.4$ mPa s; $\mathcal{C}_h \approx 4.8 \times 10^{-15}$ s	$\phi_{\text{DFN}} = 0.1$; $\mu_f = 1.0$ mPa s; $\beta_f = 9.0 \times 10^{-9}$ Pa^{-1}; $\beta_\phi = 1.0 \times 10^{-9}$ Pa^{-1}; $S_f = 1.0 \times 10^{-9}$ Pa^{-1}
Source-rate parameter	$q_{2\text{D}} = q_{\text{ref}} \approx 1.7 \times 10^{-7}$ m^2 s^{-1}	$Q_{\text{DFN}} = 6.7721 \times 10^{-8}$ m s^{-1}, split equally between the two central control volumes
Effective line-source strength	$\mathcal{S}_{\text{AQ}} = 67.7207$ Pa m s^{-1}	$\mathcal{S}_{\text{DFN}} = 67.7207$ Pa m s^{-1}
Source history	Constant from 0 to 30 yr	Constant from 0 to 30 yr

Table S5: **Matched parameters for the hydraulic diffusion benchmark in Fig. S1.** (continued).

Quantity	Adaptive-quadtree FVM	DemystiFicatioN_DFN FVM
Output interval	0.025 yr	0.025 yr
Internal time step	0.0025 yr (approximately 0.913 d)	0.0025 yr (approximately 0.913 d)
Time integration	Crank–Nicolson	Native fully implicit finite-volume update

Table S6: **Matched physical and numerical parameters for the system-level benchmark in Fig. S4.** Values in the common column were prescribed identically in the two codes. Case-specific frictional layouts refer to the velocity-weakening (VW) and velocity-strengthening (VS) parameter pairs defined in the text.

Quantity	Common value	Single-fault cycle	Parallel-fault response	Injection-driven rupture
Fault length and discretization	6 km; 50 elements per fault; 120 m per element	One fault	Two parallel faults separated by 1 km	One fault
Elastic parameters	$\mu = 30\,\mathrm{GPa}$; $\nu = 0.25$; $V_s = 3\ \mathrm{km\,s^{-1}}$; $\eta = 5 \times 10^6\ \mathrm{Pa\,s\,m^{-1}}$	Same	Same	Same
Friction reference values	$f_0 = 0.60$; $V_0 = 10^{-6}\ \mathrm{m\,s^{-1}}$; $D_c = 0.004$ m	Same	Same	Same
VW parameters	$(a, b) = (0.010, 0.014)$	Fault interior	Fault 1 interior	Fault interior
VS parameters	$(a, b) = (0.020, 0.010)$	One terminal transition	Fault 1 terminal transitions; all of Fault 2	Both terminal transitions
Tip transition	$L_{\mathrm{tip}} = 600$ m; smoothing width 200 m	One-sided	Symmetric on Fault 1	Symmetric
Regional stress	$S_{H\max} = 90$ MPa; $S_{h\min} = 46$ MPa; $S_{H\max}$ azimuth 73°	Same	Same	Same
Resolved initial stresses	$\tau_0 = 12.3022$ MPa; $\sigma_{n,0} = 49.7612$ MPa	Same	Same	Same

Table S6: **Matched physical and numerical parameters for the system-level benchmark in Fig. S4.** (continued).

Quantity	Common value	Single-fault cycle	Parallel-fault response	Injection-driven rupture
Initial pore pressure and coupling	$P_0 = 28.9$ MPa; $\alpha = 1$; no slip-induced pressure feedback	Same	Same	Same
Loading velocity V_{pl}	Case specific	$10^{-9}\ \mathrm{m\,s^{-1}}$	$10^{-9}\ \mathrm{m\,s^{-1}}$	$10^{-11}\ \mathrm{m\,s^{-1}}$
Duration	Case specific	100 yr	100 yr	70-yr spin-up + 30-yr injection
Injection	None unless specified	None	None	Central constant source, $Q = 5 \times 10^{-8}\ \mathrm{m\,s^{-1}}$, split between two central control volumes
Injection hydraulic properties	Case specific	–	–	$D = 0.1\ \mathrm{m^2\,s^{-1}}$; $k = 10^{-13}\ \mathrm{m^2}$; $\phi = 0.1$; $\mu_f = 10^{-3}\ \mathrm{Pa\,s}$; $\beta_f = 9 \times 10^{-9}\ \mathrm{Pa^{-1}}$; $\beta_\phi = 10^{-9}\ \mathrm{Pa^{-1}}$
Event-onset threshold	$V_{\max} = 10^{-3}\ \mathrm{m\,s^{-1}}$	Same	Same	Same

Table S6: **Matched physical and numerical parameters for the system-level benchmark in Fig. S4.** (continued).

Quantity	Common value	Single-fault cycle	Parallel-fault response	Injection-driven rupture
Galerkin BEM time integration	MATLAB `ode15s`; relative tolerance 10^{-5}; absolute tolerance 10^{-7}; maximum step 3×10^{7} s; initial step 10^{-3} s	Same	Same	Same
DEMYSTIFICATION_DFN time integration	Adaptive embedded Runge–Kutta; relative tolerance 10^{-5}; absolute tolerance 10^{-8}; initial step 0.01 yr; maximum step 0.1 yr	Same	Same	Same
Galerkin elastic evaluation	Analytical off-diagonal interactions; 600-point Gauss–Legendre self-interactions	Same	Same	Same

Supplementary movie captions

Caption for Movie S1. Hydraulic preparation and rupture evolution of the modeled Prague sequence. Slip-rate evolution on the three primary faults in the reference simulation shown in Fig. 2, from injection onset through Events 1–3 and subsequent relaxation. Colors indicate element slip rate on a logarithmic scale, and the bars show the maximum slip rate on each fault. Fault numbers and the injection source are marked on the map. Labels identify the three primary events and their modeled moment magnitudes. Simulation time since injection onset is displayed in years and days, with elapsed seconds additionally shown during each primary rupture. The numerical categories "Interseismic," "Nucleation / activation," and "Dynamic rupture" correspond to maximum slip rates below 10^{-4}, between 10^{-4} and 10^{-2}, and at or above 10^{-2} $\mathrm{m\,s^{-1}}$, respectively. Variable playback speed compresses long preparation intervals and expands brief rupture episodes while retaining physical timestamps.

Caption for Movie S2. Fault-network evolution across six receiver-fault prestress cases. Slip-rate evolution in the six 27-fault simulations shown in Fig. 5, from injection onset to model year 100. Panels show common shear-stress offsets of 0, +0.1, +0.2, +0.3, +0.4, and +0.5 MPa applied to receiver Faults 4–27 relative to their individual long-term mean shear stresses, arranged from left to right across the top and bottom rows. Each case preserves the primary Prague sequence. All panels share the same geometry, axis limits, and logarithmic element-slip-rate color scale. Fault numbers and the injection source are marked, and each panel reports its maximum slip rate and simulation time in years and days. Event labels and numerical slip-speed categories follow Movie S1. Playback is aligned at the onset of Event 1, while each panel retains its own physical timestamps and subsequent interevent intervals. Variable playback speed resolves the primary ruptures and later receiver-fault responses.